Cell loss disrupts mechanical homeostasis to drive retinal pigment epithelium ageing-like phenotype *in vitro*

Teodora Piskova[1], Aleksandra N. Kozyrina[2], Giedrė Astrauskaitė[2], Mohamed Elsafi Mabrouk[3], Sebastian Schepl[1], Stacy Lok Sze Yam[1], Ragul Ravithas[1], Wolfgang Wagner[3], Massimo Vassalli[2] and Jacopo Di Russo[1,4]

[1]*Institute of Molecular and Cellular Anatomy, RWTH Aachen University, Germany*
[2] *Centre for the Cellular Microenvironment, James Watt School of Engineering, University of Glasgow, Glasgow, UK*
[3]*Institute of Stem Cell Biology, University Hospital of RWTH Aachen, Aachen, Germany*
[4]*DWI-Leibniz-Institute for Interactive Materials, Aachen, Germany*

Keywords: Postmitotic epithelium, Ageing, Mechanical homeostasis, RPE, Phagocytosis

Correspondence:

Jacopo Di Russo

jdirusso@ukaachen.de

Abstract

Tissue homeostasis relies on mechanical feedback loops balanced by cell loss and proliferation. However, maintaining this balance becomes particularly challenging in postmitotic tissues, where alternative mechanisms replace compensatory proliferation. In the postmitotic retinal pigment epithelium (RPE), these mechanisms include significant structural adaptations over time. Yet, how these adaptations relate to epithelial mechanical homeostasis and age-associated functional decline remains poorly understood. To establish the relationship between structural changes, mechanical homeostasis and function, we developed an *in vitro* reductionistic model mimicking age-related reduction in RPE cell density. Inducing large-scale apoptosis in postmitotic stem cell-derived RPE monolayers recapitulates structural hallmarks of aged tissue, such as reduced cell height, shortened microvilli and cytoskeletal reorganisation. This new structure acquires a new mechanical equilibrium, evidenced by tissue stiffening and enhanced junctional contractility. Functionally, the monolayers display impaired vision-supporting phagocytosis of photoreceptor outer segments. Mechanistically, modulation of actin nucleators, Arp2/3 and formins, demonstrates that apicolateral monolayer deformation is critical for phagocytosis and may be compromised in aged RPE. Our findings suggest that a shift in mechanical homeostasis due to cell loss is a major driver of age-related RPE functional decline. Importantly, we show that structural remodelling in ageing alone can compromise tissue function, independent of other stressors.

INTRODUCTION

The structure and form of a biological entity determine its function, as described by the form-function paradigm [1,2]. This paradigm applies across various length scales, from the molecular [3,4] and sub-cellular levels [5,6] to the tissue and organ levels, where proper architecture and cellular connectivity are essential for functionality [7–9]. In recent decades, alongside form and organisation, increasing recognition as key parameters influencing function and homeostasis has also been given to the mechanical properties of tissues [10–12]. These properties are determined by the cellular organisation and environment [13–15], and their regulation within a preferred range engages mechanosensitive feedback loops that sustain physiological function [16–18], a concept referred to as mechanical homeostasis [19–21]. Despite its importance, mechanical homeostasis remains poorly understood in postmitotic tissues such as the central nervous system and the retina, which must adapt structurally to naturally occurring cell death to maintain the tissue's integrity and functional state [22–25].

An emblematic example of this adaptation is the age-related changes occurring in the retinal pigment epithelium (RPE) [26]. In the retina, the RPE is located between the light-detecting photoreceptor cells and the choroid capillaries and provides vital metabolic support to photoreceptor cells [27]. In ageing, this support is challenged by the steady rate of apoptosis in RPE [28–30], which needs to be actively compensated by the remaining cells, leading to major structural changes of the tissue. These include monolayer thinning, with the average RPE cell height reported to decrease, while cell area increases [29,31,32]. Furthermore, the RPE actin cytoskeleton remodels, leading to local fibres thickening or thinning with the formation of transcellular stress fibres [33]. Finally, ageing has been shown to be associated with changes in RPE apical microvilli, which become shorter and sparser [31,34]. In temporal correlation to these structural changes, the functional ability of the RPE to support photoreceptor cells changes towards a reduced ability to phagocyte and process photoreceptor outer segments (POS) fragments, with important implications for retinal degenerative pathologies [35,36].

While it has been proposed that the age-related changes in RPE organisation stem from a time-associated reduction in cell density, direct evidence supporting this hypothesis remains elusive. Moreover, whether such alterations drive a shift in tissue mechanical homeostasis that implies functional decline remains a critical unresolved question. Notably, we have recently shown that the strength of both cell-substrate and cell-cell adhesion forces in RPE cells directly relates to their ability to phagocytose photoreceptor outer segments (POS), with higher actomyosin contractility leading to reduced phagocytic activity [21]. Finally, because rodent models and human post-mortem tissue studies cannot reveal the precise effects of reduced cell density on monolayer structure from other ageing-related processes, such as oxidative stress or extracellular matrix (ECM) remodelling, it is necessary to establish a reductionist, human-relevant *in vitro* model.

To address this knowledge and technical gap, we present an optimised *in vitro* model that employs large-scale apoptosis on demand to promote a reduction in cell density in postmitotic human induced pluripotent stem cell-derived RPE (iRPE). This density-reduced iRPE (dr-iRPE) displays structural changes such as enlarged and thinner cells with shortened apical microvilli and cytoskeleton reorganisation, alongside increased tissue stiffness, enhanced junctional contractility and a remodelled apical cortex. The mechanical changes coincide with impaired POS phagocytosis, reflected by reduced apicolateral deformation, decreased number of internalised particles and increased fragment size. Pharmacological modulation of actin nucleation allowed us to partially rescue function, suggesting that functional alteration may result from a shift in force balances within the RPE that prioritises lateral structural reinforcement instead of apical plasticity needed for POS phagocytosis.

RESULTS

Apoptosis-generated cell density reduction leads to structural remodelling in RPE *in vitro* and phenocopies structural features of the ageing RPE

Inspired by the natural reduction in cell density in RPE *in vivo* [28,30], we aimed to replicate cell density reduction *in vitro* by inducing large-scale apoptosis and to study the adaptation of the epithelium to the cell loss. To model a native RPE monolayer, iRPE was employed as a recognised and reliable model for the native tissue [37–40]. Importantly, to investigate cellular force balance, iRPE were cultured on 4 kPa soft polyacrylamide hydrogels with basement membrane-like coating, thereby recapitulating the physiological mechanical and biochemical cues of the native substrate as previously characterized [21] (Sup. Fig. 1A). In these conditions, iRPE assumes a characteristic honeycomb-like organisation, apicobasal polarisation (Sup. Fig. 1B), and arrest of proliferation (0,01 to 0,41% within 24 h) (Fig. 1A and Sup. Fig.1C). To facilitate on-demand apoptosis, on the 10th day of culture we transduced the cells with an adeno-associated virus (AAV) carrying a construct designed to promote the expression of FKBP-caspase 8 (Fig. 1B, Sup. Fig. 1D). FKBP-caspase 8 is pro-apoptotic fusion protein that can be activated on demand through AP20187-induced dimerization, initiating the cellular suicide program [41]. Therefore, after reaching a stable expression, on the 15th day, we incubated the monolayer with the compound AP20187, inducing monolayer-scale apoptosis that led to the extrusion of 2% of the cells within the observation time (Fig. 1B-C, Sup. Fig. 1E and Video 1). By the 20th day (96 hours after apoptosis completion), the iRPE monolayer showed a reduction of cell density of approximately 8% (Fig. 1D), which was not compensated by increased proliferation. In fact, we quantified significantly lower proliferation rates compared to control monolayers (Fig. 1A). As a result, the obtained monolayer was referred to as density-reduced iRPE or dr-iRPE.

Morphologically, dr-iRPE presents cells with a larger area on average (Fig. 1E, Sup. Fig. 1F and G) without experiencing any fluidification or unjamming, as evident by

cellular area distribution and shape factor (Sup. Fig. 1H and I), recapitulating morphological changes observed in human RPE ageing [29]. Furthermore, we noticed that one-tenth of cells within dr-iRPE presented transcellular stress fibres (Fig. 1F), which were also reported to occur frequently in human RPE ageing [33]. Next, we quantified the cell height in fixed and mounted samples (Fig. 1G and H), showing that dr-iRPE is significantly thinner than the controls (9.1 vs 11.6 µm), in agreement with observations from the ageing RPE [31,42]. Lastly, motivated by the documented changes of microvilli size and number in the ageing RPE *in vivo* [31,34], we evaluated ezrin as a polarity marker and microvilli organiser [43–45]. Qualitative analyses of ezrin staining revealed a distinct morphology of the cellular apices between dr-iRPE and control (Fig. 1I), which can also be quantitatively captured by the reduced protein level detected in the cells by western blot (Fig. 1J). Moreover, the examination of the microvilli length by confocal microscopy showed approximately one-third shorter microvilli in the dr-iRPE compared to the control (Fig. 1K). Based on the studies performed on Ezrin$^{-/-}$ mice [43], these observed differences strongly suggest that in the dr-iRPE conditions, the microvilli are less elaborated and more disorganised. Finally, the quantification of the active form of ezrin (phosphorylated ezrin), which connects the actin cortex to the membrane [46], revealed a significant decrease in the dr-iRPE (Fig. 1L).

To exclude the influence of the viral delivery on the observed structural changes, we included a matched viral control, which promoted the expression of GFP (GFP-iRPE) (Sup. Fig. 2A). Compared to this control, the dr-iRPE was still showing a reduced cell density and cell height (Sup. Fig. 2B, C and D), as well as significant differences in both organisation and length of ezrin-positive microvilli (Sup. Fig. 2E). Next, we addressed the observation that despite most of the cells within the monolayer expressed the reporter after transduction, only a few of the cells ultimately underwent apoptosis during the AP20187 treatment (Video 1). To exclude any possible effects of the leftover recombinant protein in the remaining cells, we included an additional ‘mixed’ control in the analyses, consisting of an iRPE monolayer made by a mixed population of transduced (10%) and naïve cells. This condition allowed us to target the caspase activation only on a subpopulation of cells (Sup. Fig. 2F and G). Interestingly, with this approach, apoptosis still caused a significant cell density and height reduction, confirming that these features are independent of the possible presence of inactive recombinant protein in the cells (Sup. Fig. 2H and I). Lastly, we asked whether the changes were induced by secondary factors released in the medium after the large-scale apoptosis induction [47]. Hence, we transferred a medium pre-conditioned by the dr-iRPE sample during and after apoptosis onto control monolayers (Sup. Fig. 2J). Nonetheless, the quantification still showed no effect of the “conditioned medium” on cell morphology, density, or height (Sup. Fig. 2K, L and M).

Altogether, we present an *in vitro* model based on cell density reduction via on-demand apoptosis, and we demonstrate that the RPE monolayer responds to large-scale apoptosis with structural adaptation. This includes the formation of transcellular actin fibres, reduced cell height, larger cell area and shorter and remodelled

microvilli. Interestingly, these cellular responses appear to result from intrinsic tissue stretching and preservation of cell volume rather than from cellular hypertrophy. Finally, our model recapitulates key morphological features of the aged RPE *in vivo*, suggesting a causal relationship between cell loss and the structural changes observed in ageing.

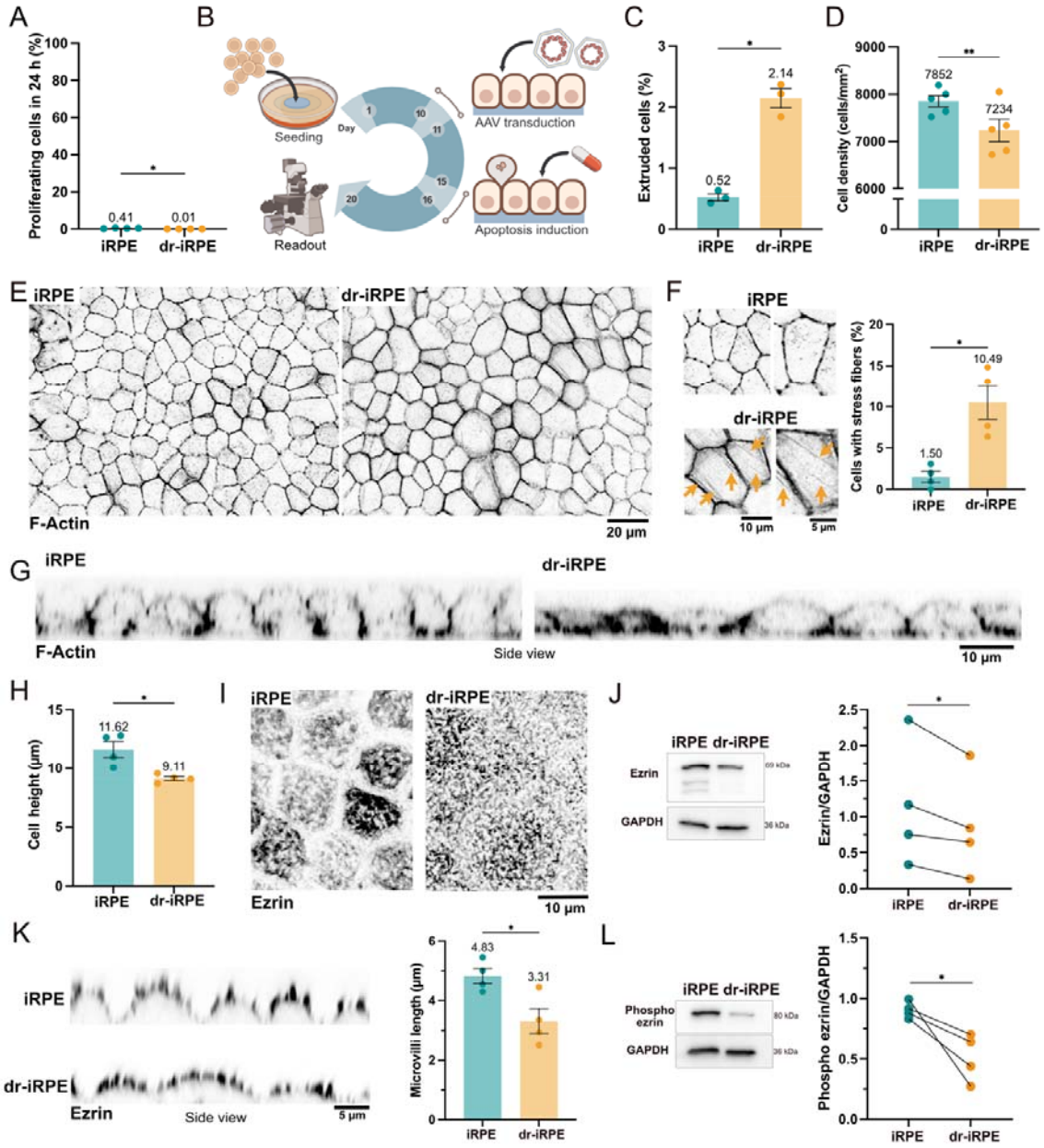

Figure 1: Structural adaptation of iRPE to cell density reduction. A: Quantification of proliferating cells within the monolayers on day 20 (n=4). **B:** Experimental timeline highlights key steps of the experiment, including cell seeding on hydrogels (day 1), AAV-mediated transduction with FKBP-casp8-encoding plasmid (day 10 to 11), apoptosis induction by the addition of the dimerising drug AP20187 (day 15 to 16), and day of read-out (day 20). **C:** Quantification of extruded cells during the apoptosis induction (n=3). **D:** Quantification of cell density within the monolayers on day 20 (n=5). **E:** Representative optical sections of iRPE and dr-iRPE stained for F-actin, which reveals cell organisation and sizes. **F:** Zoomed-in images from the iRPE and dr-iRPE with arrows indicating the local presence of transcellular stress fibres in the dr-iRPE condition (down). Quantification of cells with transcellular fibres (right, n=4). **G:** Orthogonal cross-sections of F-Actin micrographs. **H:** Quantification of cell height (n=4). **I:** Monolayer apical signal of ezrin highlighting microvilli organisation. **J:** Immunoblots showing ezrin and GAPDH as a housekeeping protein (left) and quantification of total ezrin protein from immunoblots,

normalised to GAPDH (right). Paired values from the same experiment are connected with lines (n=4). **K:** Representative orthogonal views of iRPE monolayers stained for ezrin showing the apical microvilli (left) and the quantification of their average length (right, n=4). **L:** Immunoblots showing phosphorylated ezrin and GAPDH as a housekeeping protein (left) and their quantification (right). Paired values from the same experiment are connected with lines (n=4). Datapoints represent average values per experiment (± SEM in case of bar graphs). Statistical significance in A, C, D, F, H and K was tested using a paired t-test, where *: $p<0.05$, **: $p<0.01$. Statistical significance in J and L was tested using a ratio paired t-test, where *: $p<0.05$.

Cell density reduction compromises RPE phagocytotic activity

One of RPE's main functions *in vivo* is the daily engulfment and internalisation of oxidised fragments of photoreceptor outer segments (POS), often referred to in the literature as POS phagocytosis [48] or, due to the active nature of nibbling involved, as trogocytosis [49]. Along the lines of the form-function paradigm, we asked whether the structural adaptation observed in response to cell density reduction would alter iRPE's ability to internalise POS. Thus, following an established assay [40,50], we incubated control and dr-iRPE with fluorescently labelled porcine POS fragments in the presence of bridging molecules Protein-S and MFG-E8 for 4 h (Fig. 2A). During this time, some of the fragments bound to the apical surface of the iRPE and some got internalised by the cells (Fig. 2A and B). After 3D segmentation, we used the apical actin signal to differentiate between bound and internalised fragments (Sup. Fig. 3A). Quantification revealed that the dr-iRPE exhibited significantly fewer internalised particles, both within the field of view or when normalised by cell number (Fig. 2C, Sup. Fig. 3B). Next, motivated by a reported trend of larger POS phagosomes in the RPE of aged animals [51], we further quantified the volume of the internalised photoreceptor fragments. Surprisingly, we found the average volume of internalised fragments to be larger in dr-iRPE monolayers (Fig. 2B and D). Regarding the bound particles, neither their number nor their average volume was found to be significantly different (Sup. Fig. 3C). Similar differences in internalised particle number and volume were observed in the mixed cell population subjected to cell density reduction, with fewer internalised particles and a larger average particle volume (Sup. Fig. 3E, G). Finally, the medium transfer from the apoptotic-induced samples showed no significant impact on either the internalised particle count or on the fragment volume (Sup. Fig. 3F and H).

Altogether, these data demonstrate that structurally remodelled dr-iRPE exhibit deficient internalisation of POS fragments, internalising fewer and larger fragments. By phenocopying the phagocytic deficits observed in ageing RPE, this model suggests that reduced cell density alone can drive functional decline in the remaining cells.

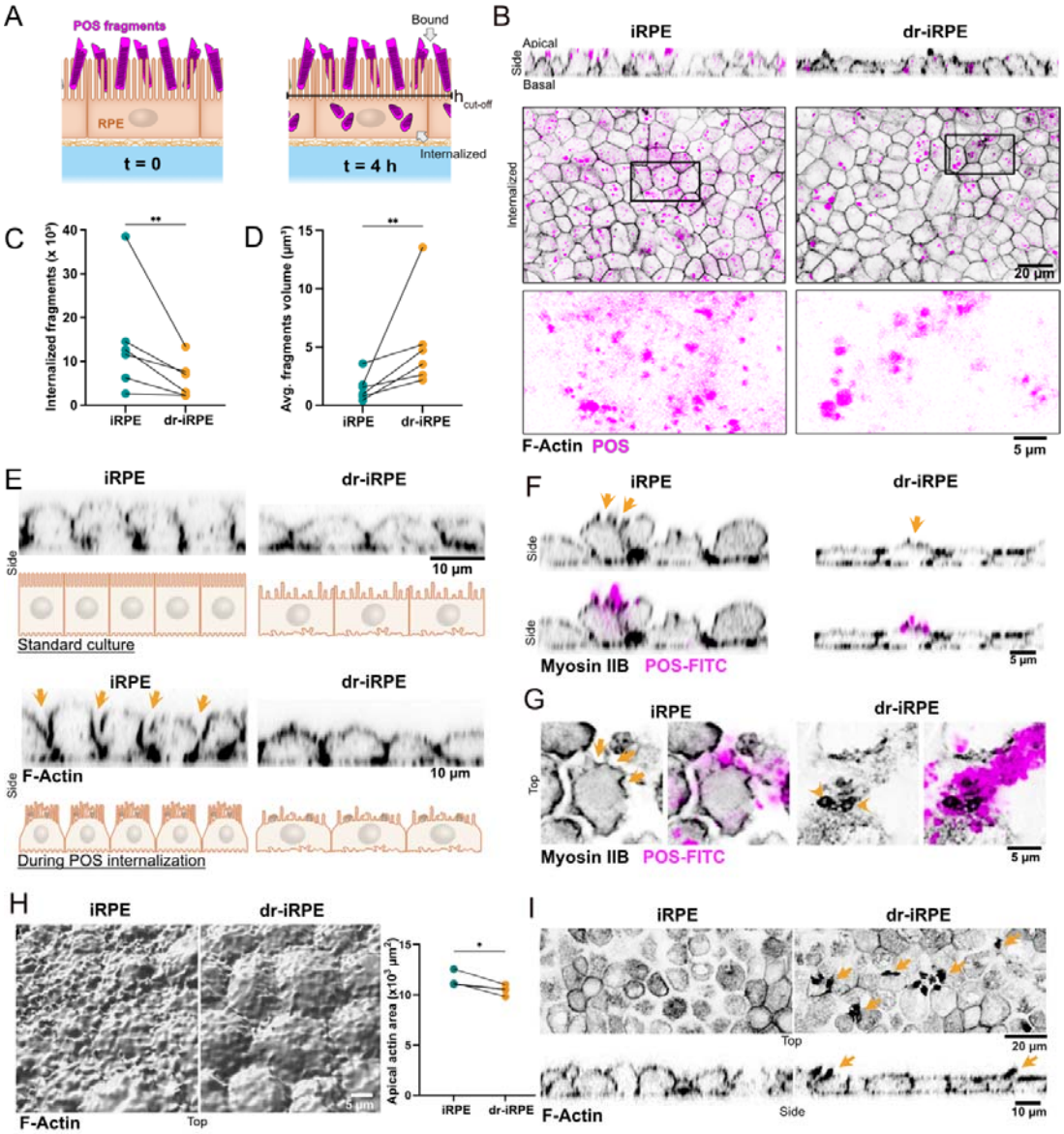

Figure 2: Density reduced iRPE shows altered internalisation of POS fragments. A: Schematics of POS fragment internalisation assay. Isolated and labelled porcine POS fragments are fed to iRPE together with bridging molecules at timepoint 0 and analysed four hours later. To distinguish between bound and internalised fragments, we define a cut-off height. **B:** Representative orthogonal cross-sections and single optical slices of iRPE and dr-iRPE at t = 4 h. Zoom-in of the POS signal from the inlet showcases the size of the fragments. **C:** Quantification of fragments internalised within the time of the assay. Values are shown as times thousand per field of view (n=6). **D:** Quantification of the average volume of internalised fragments. Data points represent average values per experiment (n=6). Statistical significance in C and D was tested using a ratio paired t-test, where **: $p<0.01$. **E:** Representative orthogonal cross-sections of F-actin labelled monolayers in a standard culture condition vs during the POS internalisation assay. Images are not paired. Schematic illustration and arrows highlight the distinct cross-sectional morphology of cells, with control cell bodies bulging out above the level of cell-cell junctions. **F:** Representative orthogonal cross-sections of Myosin IIB labelled monolayers and FITC-labelled POS fragments. Myosin IIB is enriched in proximity to the POS (arrows). **G:** Representative apical view of iRPE cells in control and density reduced condition, stained for Myosin IIB during internalisation of POS-FITC. In contrast to many small phagocytic cups localised apically and laterally in iRPE (arrows), dr-iRPE shows fewer apical-only cup-like structures with more localised myosin signal (arrowheads). **H:** Representative 3D segmentation of apical F-actin surface of monolayers during internalisation assay (left) and quantification of apical actin area within the same field of view (right). Datapoints represent average values per experiment (n=3). Statistical significance was tested using a ratio paired t-test, where *: $p<0.05$. **I**: Representative apical and orthogonal cross sections of F-actin-labelled monolayers during internalisation. Arrows indicate the presence of protruding actin-rich structures in dr-iRPE.

Cell density reduction leads to altered actomyosin plasticity and mechanical properties

POS phagocytosis relies on the active remodelling of the apical actin network, which plays a crucial role in fragment internalisation and phagosome size [40,49,50]. Actin dynamics are essential throughout the process, guiding key steps from initial binding and ensheathment to the final scission of the phagosome [48,52]. Thus, we examined the morphology of the apical actin during internalisation, on a few-cell scale in our 3D segmentation and on a larger monolayer scale. In the side view, we noticed the apical actin of control iRPE monolayers experienced a substantial deformation during the internalisation, such as bulging and enlargement of the protruding cell portion above the cell junctions and clear formation of myosin IIB-positive cups (Fig. 2E-H). In contrast, dr-iRPE did not experience much evident deformation, and phagocytotic cups were less resolved (Fig. 2F and G). Next, we noticed that cells in the dr-iRPE displayed a different apical actin topography compared to the control, having an overall smoother surface, as quantified by area per field of view (Fig. 2H). Finally, on the monolayer scale, we noticed that the dr-iRPE frequently presented large actomyosin-rich apical structures (Fig. 2G and I, Sup. Fig. 4A and B), which were absent in iRPE samples.

These observations suggest that iRPE cells in the density-reduced condition exhibit altered ability in remodelling their actomyosin cytoskeleton when internalising POS fragments. Consequently, we wondered whether the differences stemmed from distinct patterns of actin-cytoskeleton-related signalling. Hence, we examined the myocardin-related transcription factor A (MRTFA), which is known to regulate actin-associated signalling [53]. We observed a short-term translocation of MRTFA into the nucleus at day 17, shortly after the large-scale cell loss, which went back to levels comparable to the control at day 20, or the day of the read-out (Fig. 3A and B). This demonstrates that the cell density reduction leads to a transient transcriptional adaptation, possibly conveying the observed structural remodelling of dr-iRPE. We then examined the mRNA expression of actin-associated proteins after bulk RNA sequencing (Fig. 3C, Sup. Fig. 5A). Examining more precisely the expression of these proteins showed an array of significantly differentially expressed actin-related genes in the dr-iRPE. Upregulated genes in dr-iRPE contained genes related to actin branching, polymerisation, depolymerisation, and crosslinking (*ARPC2, PFN1, FHOD3, INF2, CFL2, ACTN1, FSCN1, FLNA*). Downregulated genes included ezrin and the formins *DIAPH1, DIAPH2, DAAM1* and *DAAM2* (Fig. 3D and E). Next, to further assess the parallel between our model and ageing RPE, we compared global gene expression changes in iRPE and dr-iRPE with those reported in ageing RPE from two independent studies [54,55] (Sup. Fig. 5 B-D). Considering the significant differences from our reductionist approach and *in vivo* human data, as well as the differences between the results of the studies, it is worth noting that our model may mimic further aspects of RPE ageing besides the actomyosin remodelling discussed in this work.

Altogether, these insights point to a distinct signature of actin-associated proteins in dr-iRPE that implies altered actomyosin network organisation, consistent with the observed changes in subapical F-actin topography. Such reorganisation may prevent the formation of the prominent apical deformations or bulges required for efficient phagocytosis, instead promoting the emergence of localised actin-rich structures.

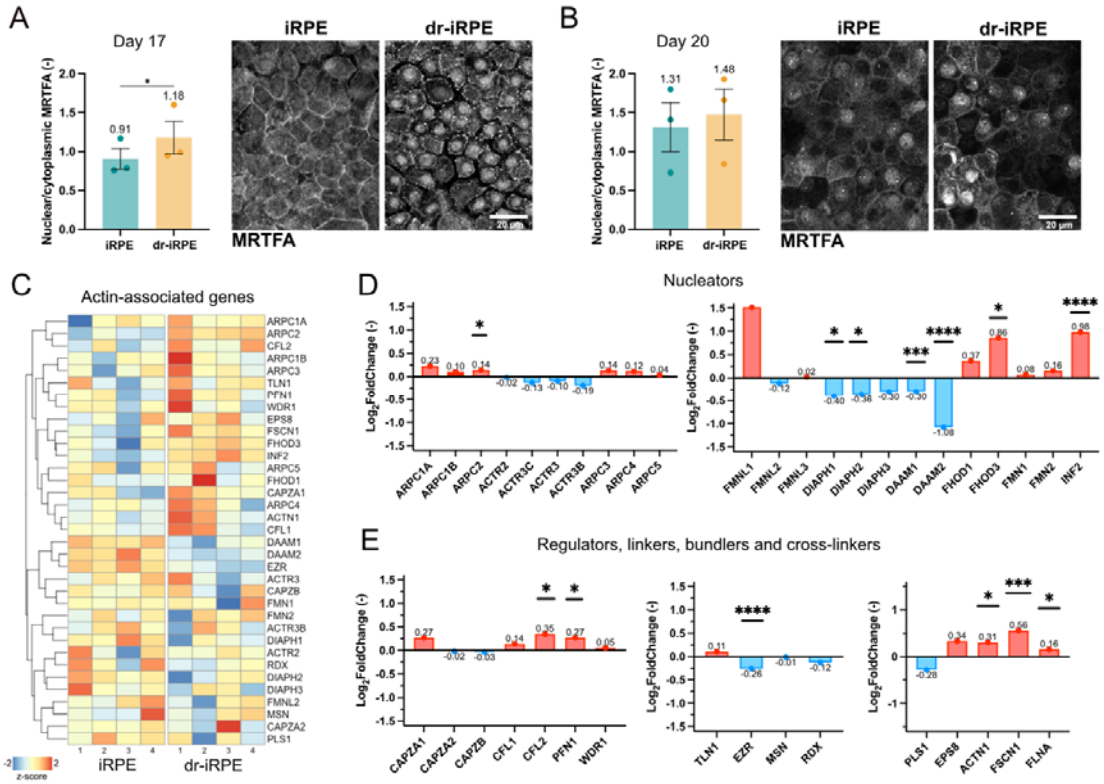

Figure 3: A different fingerprint of actin-associated proteins in density reduced iRPE. A: Quantification of nuclear to cytoplasmic MRTFA fluorescence intensities and representative micrographs of MRTFA staining one day after apoptosis induction (day 17). **B:** Quantification of MRTFA fluorescence intensities and representative micrographs of MRTFA staining on the day of readout (day 20). Datapoints in A and B represent average values per experiment ± SEM originating from n=3 independent experiments. Statistical significance was tested using a ratio paired t-test, where *: $p<0.05$. **C:** Hierarchically clustered heatmap of RNA transcript counts of actin-related proteins from n=4 independent experiments of iRPE vs dr-iRPE samples. **D:** Graphs showing the Log2Fold change in RNA transcript expression of branched (left) and linear (right) actin nucleator proteins for dr-iRPE vs. iRPE. **E:** Graphs showing the Log2Fold change in RNA transcript expression of actin assembly/disassembly regulators (left), actin membrane linkers (middle) and crosslinkers and bundlers (right) for dr-iRPE vs. iRPE. Differentially expressed genes in D and E are marked with *: $p_{adj}<0.1$, **: $p_{adj}<0.01$, ***: $p_{adj}<0.001$, and ****: $p_{adj}<0.0001$ as a result of the use of negative binomial generalised linear models and Wald test.

As we previously showed that RPE mechanical equilibrium influences the epithelium phagocytotic activity [50], we sought to determine whether the observed actin network remodelling would alter the mechanical properties of dr-iRPE. To characterise the viscoelastic properties of the monolayer as a multicellular system, we conducted nanoindentation using a spherical tip with a diameter of 20 µm, allowing to probe a contact area of approximately 10 µm in diameter (Fig. 4A, Sup. Fig. 6A, Video 2). This approach allowed us to measure the Effective Young's modulus of the uppermost 2.5 µm of the monolayer, which approximately corresponds to the apical-most 9% of the cell height (average height of live iRPE is 27.8 ± 0.6 µm). The

Effective Young's modulus of dr-iRPE was roughly one-third higher (694 Pa vs 513 Pa), pointing to a stiffer tissue (Fig. 4B). Next, using the same nanoindentation setup, we quantified both storage and loss moduli at different probing frequencies to characterise the monolayer viscoelasticity [56]. With this approach, we found a significant increase in the storage modulus of the dr-iRPE while the loss modulus remained unchanged (Fig. 4C, Sup. Fig. 6B). Similar differences were observed when dr-iRPE was compared to the virus control or when the condition with mixed cell population was analysed without or with cell extrusion (Sup. Fig 6D and E). In the latter case, the differences in stiffness and storage modulus were smaller and only apparent at the lower probed frequencies (1 and 2 Hz). Lastly, medium transfer controls seemed to experience softening rather than stiffening, excluding an effect of apoptotic debris on the observed stiffening in dr-iRPE (Sup. Fig. 6F). Collectively, these measurements revealed a reinforced cellular interconnectivity that results in a less deformable monolayer, i.e. stiffer, as well as more elastic, suggesting an actomyosin-based reinforcement [57].

As mechanical properties and contractility are often linked [58,59], we examined the levels of phosphorylated myosin light chain 2 (pMLC2) to obtain a general idea about actomyosin contractility [60]. Immunoblotting revealed general increased levels of pMLC2 in dr-iRPE (Sup. Fig. 6C), pointing to overall higher actomyosin contractility, especially localised at the cell-cell junctions as shown by immunofluorescent staining (Fig. 4D and D^{I}). This observation was further supported by enrichment of vinculin at the cell-cell and at the tricellular junctions (Fig. 4E and E^{I}), pointing to higher contractile force at cell-cell junctions [61].

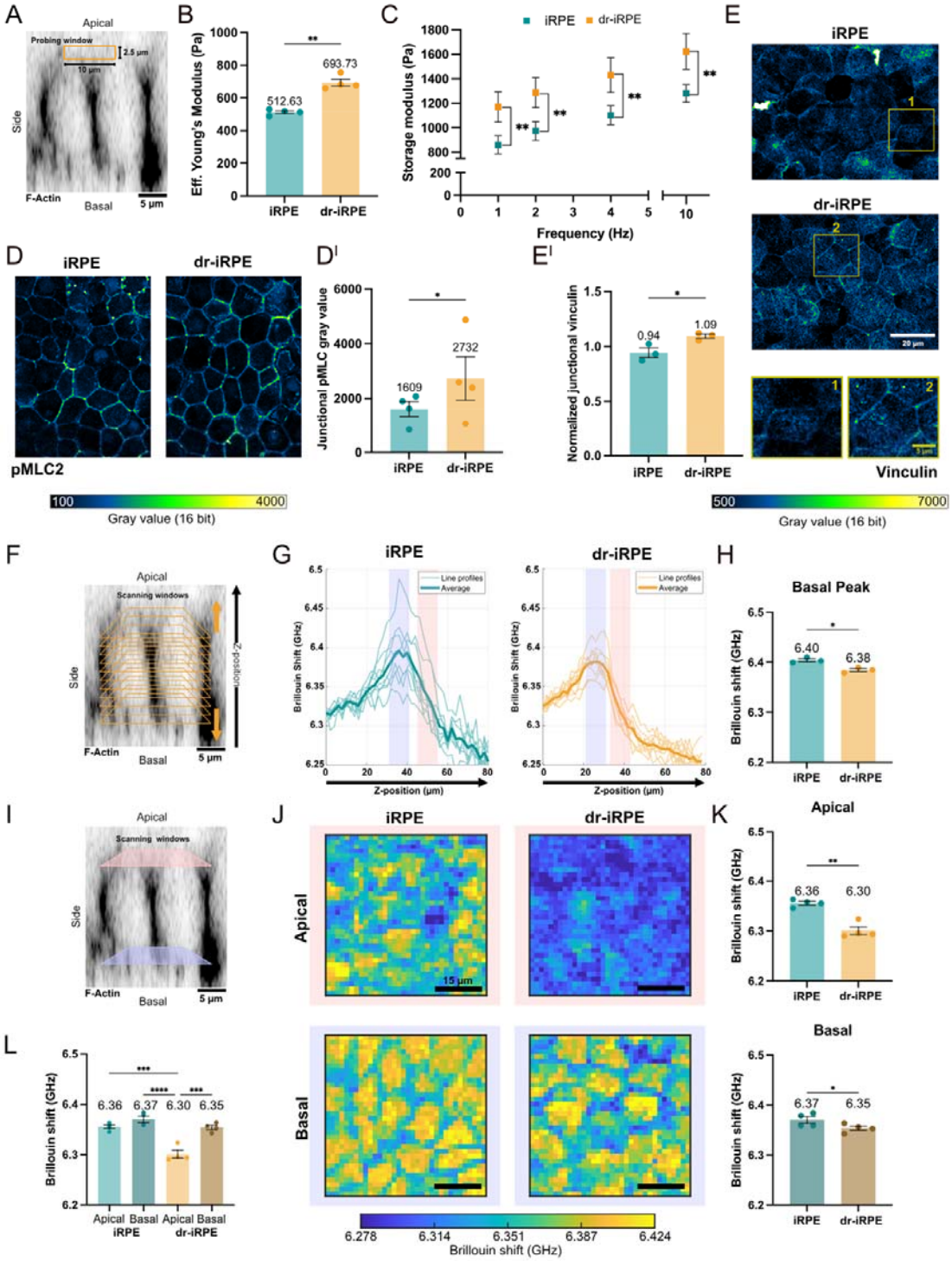

Figure 4: Density reduced iRPE presents a new biomechanical state. A: Image illustrating the probing window (10 x 2.5 µm) during nanoindentation on an orthogonal cross-section of F-Actin-labelled live iRPE. **B:** Average Effective Young's Modulus measured by nanoindentation scans in iRPE and dr-iRPE (n=4). **C:** Average storage modulus at different oscillation frequencies (n=4). **D:** Representative images of pMLC2-labelled iRPE monolayers with grey values represented in the colour bar. **D'**: Quantification of junctional pMLC2 signal (n=4). **E:** Representative images of vinculin-labelled iRPE monolayers with annotated regions enlarged. **E':** Quantification of junctional fluorescence signal of vinculin normalised to cytoplasmic fluorescence signal (n=3). **F:** Image illustrating the geometry of low-resolution Brillouin z-scans on an orthogonal cross-section of F-Actin-labelled live iRPE. **G:** Representative line profiles of the z scans showing the Brillouin shift values starting from the hydrogel, across the iRPE monolayers and reaching into the cell medium. Averages of z-scans are represented with thicker lines. Highlighted in light lilac and salmon are the approximate basal and apical cell regions, respectively. **H:**

Quantification of Brillouin shift values obtained by fitting the peaks of the curves shown in **G** (n=3). **I:** Image illustrating high-resolution 2D raster scan windows on an orthogonal cross-section of F-Actin-labelled live iRPE. **J:** Representative Brillouin shift maps obtained from the 50 x 50 μm apical and basal scans of the iRPE monolayers. **K:** Quantification of mean Brillouin shift values from 50 x 50 μm regions of interest recorded in apical and basal regions in iRPE monolayers. **L**: Comparative bar plot of apical and basal Brillouin shifts in iRPE and dr-iRPE cells. Data points represent average values per experiment ± SEM. Statistical significance in **B** and **C** was tested using a paired t test, in **D**^{I} and **E**^{I} – using a ratio paired t test, where *: $p<0.05$, **: $p<0.01$, ***: $p<0.001$ and ****: $p<0.0001$. Statistical significance in **H** and **K** was tested using a paired t-test, and in **L** using a one-way ANOVA, where *: $p<0.05$, **: $p<0.01$, ***: $p<0.001$, and ****: $p<0.0001$.

Nanoindentation enabled us to characterise the biomechanical properties of the RPE from the apical side. Our indentation setup was designed to probe multicellular length scale deformation, where the indentation of the 20 µm tip at the selected depth is counteracted by intercellular junctions [62] (Fig. 4A, Sup. Fig. 6A, Video 2). To characterise subcellular mechanical properties of the RPE monolayer non-invasively, i.e., independently from intercellular adhesion, we applied Brillouin micro-spectroscopy. Here, the detection of photons, inelastically scattered by thermally-induced acoustic phonons, enables the probing of viscoelastic properties within the sample at microscale resolution [63]. Using Brillouin microscopy, we first performed low-resolution z-scans through iRPE and dr-iRPE monolayers, including the surrounding hydrogel and medium (Fig. 4F). These line profiles revealed the presence of a peak in the Brillouin shift, corresponding to the cellular basal side, which gradually decreased towards the apical cell region (Fig. 4G). The quantification of fitted peak values of these line profiles revealed significantly lower Brillouin shift in dr-iRPE compared to iRPE (Fig. 4H). Moreover, based on the peaks shown in Figure 4G and confirmed by live-cell brightfield imaging, we identified the apical and basal z-levels for conducting 2D high resolution raster scans (Fig. 4I). The 2D raster scans (50 x 50 µm) revealed mechanical compartmentalisation into areas with different Brillouin shifts, which may correspond to cellular and intercellular regions (Fig. 4J). Notably, this compartmentalisation was much more evident at the basal sides. The quantification of the mean Brillouin shifts revealed a difference between the conditions, with dr-iRPE cells showing lower average values at the apical (6.30 vs 6.36 GHz) and basal (6.35 vs 6.37 GHz) sides of the cells (Fig. 4K). Interestingly, when comparing apical and basal shifts within the same conditions, dr-iRPE cells showed significantly different apical shifts compared to basal, which was not the case in iRPE (Fig. 4L). As the Brillouin shift reflects cytoskeletal organisation and water content[63–65], this supports the idea that the apical sides of the cells undergo the most pronounced reorganisation in dr-iRPE. This is consistent with microvilli and apical actin remodelling observed in dr-iRPE, i.e., transcellular stress fibres and F-actin surface topography.

As the intercellular junctions showed an increased pMLC2, thereby an increased contractility and stiffness, we sought to isolate the shifts of “cell edges" from those of "cell bodies". As this distinction was not clear in the apical scans, we performed the analysis on the basal sides, where the distribution of shift values revealed two distinct modes (Sup. Fig. 7A and B). Quantification based on segmented Brillouin shift plots shows that, regardless of the experimental condition, the interstitial regions of the monolayer (“cell edges”) consistently exhibit lower shifts than the cell cores (“cell bodies”). This also confirms a trend toward reduced core shifts in dr-iRPE

independently of the interstitium (Sup. Fig. 7C and D). Notably, the shift quantified at the interstitium was unexpectedly lower than the cell bodies, likely reflecting the absence of well-defined intercellular junctions at the basal side, and instead, the presence of loosely interdigitated basal membranes, as seen in F-actin staining (Sup. Fig.7E).

Altogether, biomechanical characterisation at the two different length scales showed that, in addition to the structural and functional adaptation, the reduction of cell density causes RPE to adopt a different mechanical state. This mechanical state is associated with increased contractility at the apical intercellular junctions, which confers a stiffer and more elastic tissue, as evident by the nanoindentation. Brillouin shift analyses at the subcellular level also confirmed distinct mechanical states between the two conditions, most pronounced at the apical surface. Taken together, this apical prevalence of the mechanical changes may result from the intimate link between the epithelial junctional complex and the organisation of the apical domains, which in the case of the RPE may create a mechanical feedback loop between tissue integrity and function.

Modulating actin remodelling differentially impacts POS phagocytosis

Motivated by our observations on cortical actin topography, mechanics, and the differential expression of actin-related regulators, we aimed to directly investigate the cause-effect relationship between POS internalisation and actin remodelling. To this end, we targeted actin nucleation, a key process influencing cortical thickness and membrane tension [66]. For the experimental design, we considered the upregulation of Arp2/3 subunit mRNA expression and the downregulation of several formins in dr-iRPE (Fig. 3D), along with the distinct actin structures observed during internalisation. Dr-iRPE exhibited a larger, flatter actin surface topography (Fig. 2H), suggesting an abundance of heavily branched actin, similar to that found in lamellipodia. In contrast, control samples displayed more numerous, smaller, and protruding actin structures (Fig. 2H), resembling filopodia, which are characterised by linear actin cores and highly dependent on formin activity [67]. Based on these findings, we inhibited Arp2/3 activity using the compound CK-666[68] and inhibited formin activity using the compound SMIFH2 [69].

Formin inhibition in iRPE did not affect the cell height but significantly stiffened the monolayer on a tissue level (Sup. Fig. 8A, B). In dr-iRPE, the inhibition did not produce a change in cell height, but led to a softer monolayer (Sup. Fig. 8C, D). When tested for the POS fragments internalisation, the quantification showed a highly variable effect on the number of internalised particles, which nevertheless showed an overall significant reduction in the number of both internalised and bound POS fragments (Fig. 5A and B; Sup. Fig. 8E and F). In contrast, no difference was detected in SMIFH2-treated dr-iRPE (Sup. Fig. 8G). Next, we quantified the fragments' size, which was significantly affected by SMIFH2 only in iRPE, resulting in larger fragments on average (Fig. 5A and B, Sup. Fig. 8H). Since SMIFH2 affected internalisation of POS only in iRPE, we further analysed 3D-segmented actin and

monolayer deformation during internalisation. SMIFH2-treated iRPE monolayers displayed a smoother apical actin topography; however, this was not captured by the quantification of the total apical actin area (Fig. 5C; Sup. Fig. 8I). Furthermore, SMIFH2-treated iRPE monolayers also bulged out upwards similarly to untreated controls, but showed denser F-actin signal at the junction, suggesting a lateral reinforcement comparable to dr-iRPE (Fig. 5D). In addition, the bulging cells showed a more irregular apical morphology (Fig. 5D).

Although SMIFH2 is widely accepted as a reliable formin inhibitor, it has been reported to have a concentration-dependent off-target effect on Myosin II activity [70]. To evaluate whether the effects observed with 20 µM SMIFH2 were not due to partial Myosin II inhibition, we conducted SMIFH2 treatments across a range of concentrations (5–100 µM). We then assessed iRPE and dr-iRPE monolayers for changes in stiffness and phagocytic activity (Sup. Fig. 8J, L, N, P, R and T). As a positive control for Myosin II inhibition, we used blebbistatin (Sup. Fig. 8K, M, O, Q, S and U). In iRPE, stiffness quantification confirmed a significant monolayer stiffening with 20 µM SMIFH2, whereas blebbistatin treatment induced an expected softening as cellular contractility is reduced (Sup. Fig. 8J and K). Differently, dr-iRPE treated with SMIFH2 displayed an overall softening effect, most prominent at 100 µM, consistent with the trend observed following blebbistatin treatment (Sup. Fig. 8L and M). Finally, analyses of the POS internalisation process revealed that both SMIFH2 at all concentrations and blebbistatin reduced the number of internalised POS particles in iRPE. Still, only the low concentrations of SMIFH2 (5 and 20 µM) led to increased average phagosome size, while blebbistatin did not affect fragment size (Sup. Fig. 8N-Q).

In dr-iRPE, SMIFH2 significantly reduced the number of internalised particles only at 5 µM with no effect at higher concentrations, whereas blebbistatin reduced it (Sup. Fig. 8R, S). Average phagosome size was clearly reduced by SMIFH2 treatment in dr-iRPE, in opposite direction to iRPE (Sup. Fig. 8T), while blebbistatin did not affect the phagosome size (Sup. Fig. 8 U). Overall, while we cannot fully exclude the possibility of minor off-target inhibition of Myosin II by 20 µM SMIFH2, we are confident that Myosin II inhibition does not drive our results. This confidence stems from the clear differences in trends for iRPE and dr-iRPE regarding both stiffness and internalised POS number and volume, as well as the contrasting effects seen with blebbistatin treatments.

The inhibition of Arp2/3 using CK-666 in iRPE did not change the cell height or stiffness, whereas in dr-iRPE, the treatment led to a slightly increased cell height (Sup. Fig. 9A and B), but no significant changes in monolayer stiffness (Sup. Fig. 9C and D). During phagocytosis, no effect was detected when iRPE were treated, but in dr-iRPE, the treatment led to an increased number of internalised particles (Fig. 5E and F; Sup. Fig. 9E and G), while the average internalised particle size and the number of bound particles remained comparable (Fig. 5E, G, Sup. Fig. 9F and H). As the phagocytic process was affected only in dr-iRPE, we proceeded to analyse the morphology of the 3D-segmented cortical actin during internalisation. The analyses

showed the occasional presence of thinner and longer ruffles (Fig. 5G), which resulted in a significant increase in the quantified apical actin area (Sup. Fig. 9I). Furthermore, orthogonally, the treated dr-iRPE showed some degree of ‘bulging’ during phagocytosis, which was more pronounced than in the untreated dr-iRPE (Fig. 5H).

Overall, these results demonstrate that modulating actin cytoskeleton remodelling by interfering with actin nucleation effectively altered cortical actin responsiveness during internalisation. These manipulations were sufficient to replicate or rescue differences in photoreceptor internalisation observed in dr-iRPE. Particularly, Arp2/3 activity appears to be related to cell ‘bulging’, modulating apical actin area and cell height, which impacts the number of internalised particles, while formins activity modulates tissue-level stiffness, affecting both the number and size of the internalised particles.

These insights strongly indicate that dr-iRPE cells establish a new mechanical equilibrium, in which the actin cytoskeleton acts as a critical link between tissue structure, mechanics, and the execution of phagocytosis. The altered organisation of the actomyosin network enhances contractility at cell-cell junctions, and simultaneously reduces the capacity for apical remodelling required for the formation of phagosomes. We therefore conclude that, in response to reduced cell density, the RPE monolayer reroutes actin-related processes toward reinforcing tissue integrity. This shift diminishes the plasticity of the actin-myosin network, which is essential for efficient POS phagocytosis (Fig. 6).

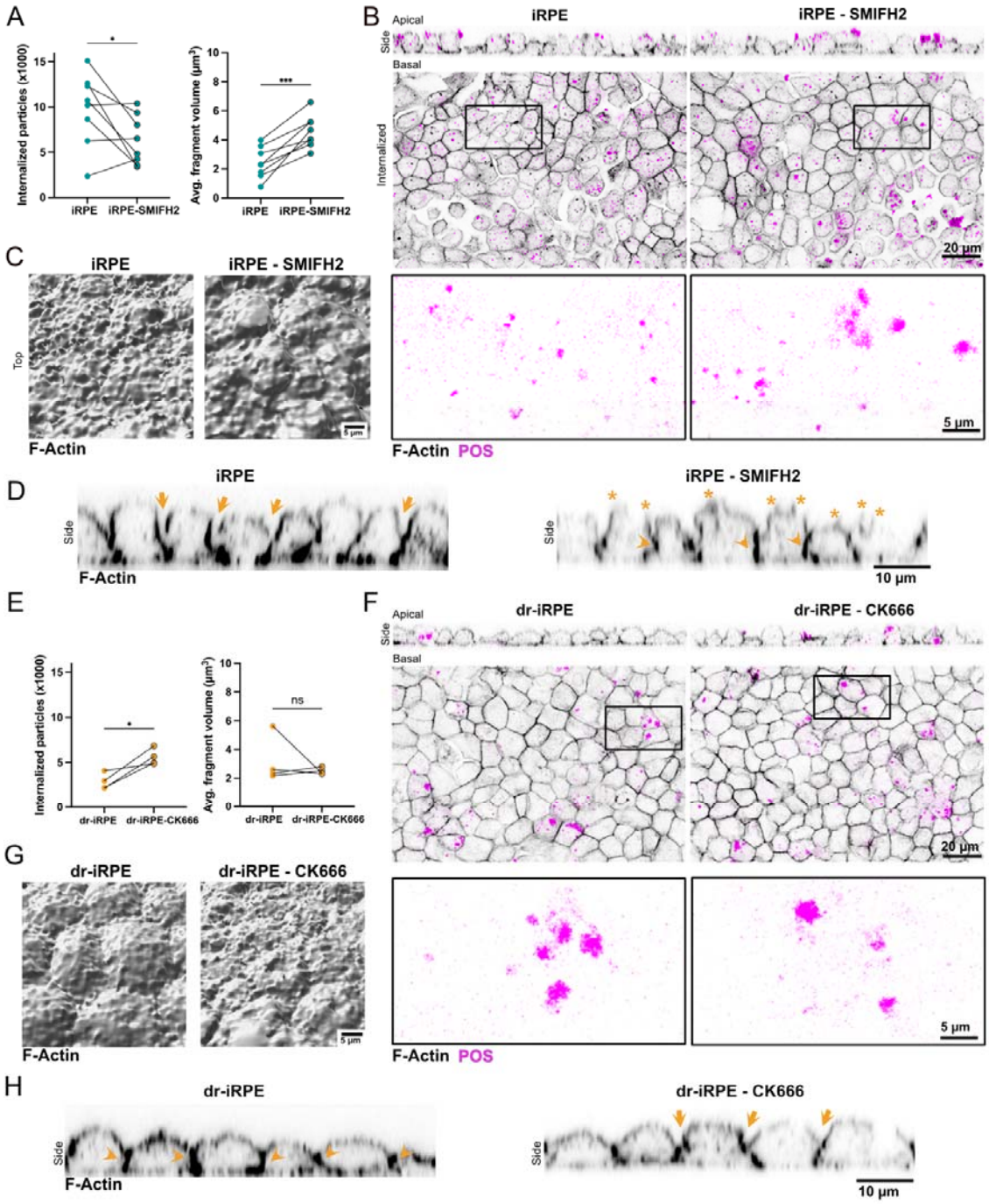

Figure 5: Actin modulation via nucleator inhibitors affects internalisation of photoreceptor outer segments. A: Number of internalised fragments (left) and their average volume (right) for iRPE vs iRPE treated with 20 µM SMIFH2 (n=8). **B:** Representative orthogonal cross-sections and single optical slices of iRPE and SMIFH2-treated iRPE at t = 4 h. Zoom-in of the POS signal from the inlet showcases the size of the fragments. **C:** Representative 3D segmented apical F-actin surface of monolayers during POS internalisation assay for iRPE vs SMIFH2-treated iRPE. **D:** Representative orthogonal cross-sections of F-actin labelled monolayers during POS internalisation assay of untreated and SMIFH2-treated iRPE. Arrows indicate the junctional remodelling to induce cell bulging, arrowheads indicate the junctional reinforcement, and stars highlight apical irregularities. **E:** Number of internalised fragments (left) and their average volume (right) for dr-iRPE vs dr-iRPE treated with 500 nM CK-666 (n=4). **F:** Representative orthogonal cross-sections and single optical slices of dr-iRPE and CK666-treated dr-iRPE at t = 4 h. Zoom-in of the POS signal from the inlet showcases the size of the fragments **G:** 3D segmented apical F-actin surface of monolayers during POS internalisation assay for untreated vs CK666-treated dr-iRPE. **H:** Representative orthogonal cross-sections of F-actin labelled monolayers during photoreceptor fragment internalisation assay of untreated and CK666-treated dr-iRPE. Arrows indicate the junctional remodelling to

induce cell bulging, while arrowheads indicate the junctional reinforcement. Datapoints represent average values per experiment. Statistical significance was tested using a ratio paired t-test, where *: $p<0.05$.

DISCUSSION

In this work, we present an *in vitro* model that recapitulates structural and functional features of the aged RPE. The model is inspired by the natural loss of cells through apoptosis within the native RPE during ageing. Comparing dr-iRPE with iRPE, we demonstrate significant changes in biomechanical features that evidence a shift in RPE mechanical equilibrium related to the structural remodelling to accommodate the reduced cell density. Most importantly, this shift has implications for the function of POS internalisation, potentially leading to impaired tissue performance. We identify remodelling of the actin cytoskeleton as a key factor mediating both the structural tissue adaptation to cell loss and the observed functional differences, suggesting that tissue preservation may be prioritised at the expense of functional trade-offs in ageing RPE. Ultimately, this structural adaptation disrupts the actomyosin machinery's ability to effectively remodel, thereby compromising efficient phagosome formation and POS phagocytosis (Fig. 6).

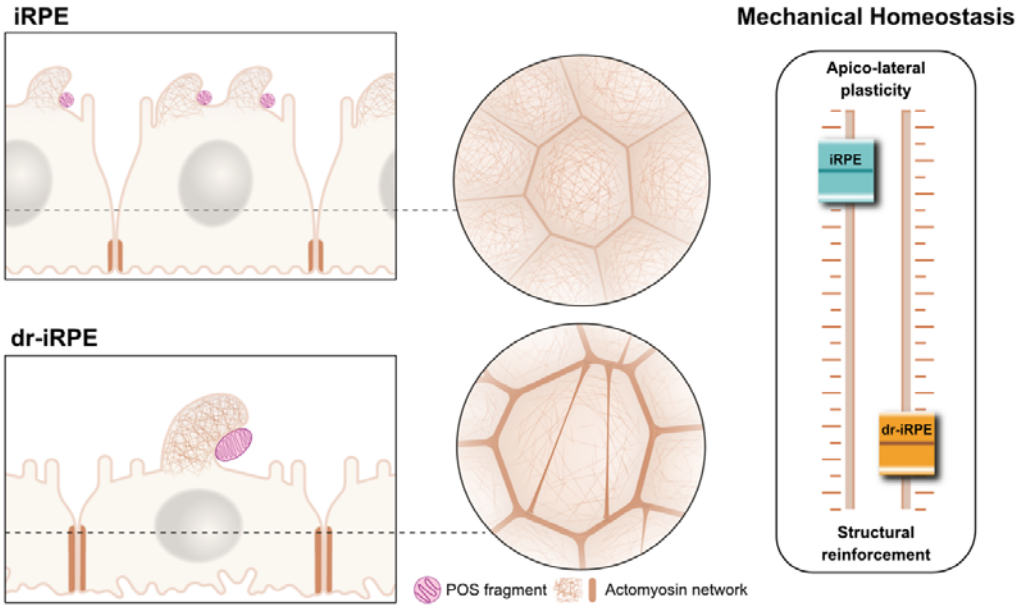

Figure 6: Cell density reduction leads to a shift in RPE mechanical homeostasis. The density reduction in iRPE leads to structural remodelling and biomechanical alterations that recapitulate the tissue architecture of the aged native RPE, suggesting a shift in mechanical homeostasis. These changes correlate with a reduced number of internalised POS fragments, which are larger in size, highlighting functional decline. Actin cytoskeleton remodelling mediates structural reinforcement and functional alteration, suggesting a trade-off where tissue structural preservation compromises the apico-lateral plasticity essential for phagosome formation and POS phagocytosis.

Ageing is a multifactorial phenomenon that impairs the capacity for dynamic homeostatic adjustments [71]. Only recently has the scientific community acknowledged altered mechanical properties as a hallmark of ageing [72], raising interest in mechanobiological studies in ageing. With the aim of studying the effect of reduced cell density on the structural and functional adaptation of RPE, our model highlights the importance of tissue organisation and mechanical properties in ageing.

By using epigenetically 'young' [73] cells derived from human induced pluripotent stem cells (hiPSCs), which have undergone rejuvenation-associated reprogramming, we reduced the complexity down to examining how tissue architecture alone impacts mechanical homeostasis and functional capacity, putting aside more complex aspects of biochemical signalling such as oxidative stress. In this system, we were able to recapitulate structural aspects identical to reported remodelling of the aged RPE, such as cell height reduction [31], shortening of the apical microvilli [74] and presence of actin stress fibers [33] by only reducing cell density. This remodelling is possible due to the nearly postmitotic nature of iRPE cells, which cannot use compensatory proliferation as a homeostatic mechanism, but are believed to rely on compensatory cellular hypertrophy [75,76]. We noted that cellular 'hypertrophy' in our model is not merely cell volume enlargement, but 'tissue stretching from within'. We observed cell area enlargement paired with cell height reduction, pointing to individual cell volume conservation, which may enrich the current notion of compensatory hypertrophy in postmitotic epithelia [76]. Individual cell area enlargement could also explain the observed microvilli shortening, as microvilli provide membrane reservoirs capable of unfolding to facilitate cell shape changes or to buffer mechanical stress [77,78]. In light of the cell density changes in RPE pathologies such as proliferative vitreoretinopathy and age-related macular degeneration[79,80], future studies should explore the relationship between the degree of cell loss and the structural, functional or cell-cycle-related adaptations.

The changes induced by cell density reduction are also paired with a shift in the range of mechanical equilibrium. This shift is evidenced by multicellular length-scale stiffening and increased elasticity, with softening at the apical side at the subcellular length scale. Tissue stiffening, in particular increased elasticity, has been reported as a response of epithelial cells to stretch [77,81], at least in the short term. In our system, the mechanical changes are observed in the long term, four days after the apoptosis-mediated deformation. While these data reveal how RPE cells *in vitro* compensate for large-scale cell loss, the situation *in vivo* is undoubtedly more complex to decipher. Multiple factors influence native tissue during ageing, making a direct comparison between our reductionistic model and physiological RPE ageing premature. Nevertheless, alterations in actin cytoskeletal organisation have been reported in aged RPE [33], supporting the notion that changes in mechanical homeostasis, including tissue stiffening, also occur *in vivo*. Such adaptation may arise from reduced cell density and the resulting need to reinforce tissue integrity. This is particularly evident in the formation of transcellular actin stress fibres, observed both in our model and in aged native tissue [33]. In fact, the occurrence of transcellular actin stress has been reported as a sign of junctional remodelling [82] and limiting cell size or elongation during morphogenesis [83]. Moreover, the strengthening of cell-cell junctions is a known mechanism to support cells in resisting forces [84]. Interestingly, the non-invasive probing technique of Brillouin microscopy revealed a mismatch between tissue reinforcement and apical cortex remodelling. Although the results of indentation measurements cannot be directly compared to light-based measurements [63,64,85], the observed lower Brillouin shift may be explained by significant changes in

the apical cortex composition and in the apical microvilli, which are rich in actin and tubulin filaments. These filaments enhance the Brillouin shift due to their structural stiffness compared to the underlying cell [65]. A more elaborate apical cortex may also possess a different level of hydration, which has recently been shown to be a crucial factor affecting Brillouin, but not indentation-based measurements[64]. Furthermore, differential remodelling of the apical and lateral cortical actin networks is likely, as is known to happen during morphogenesis [86]. Notably, the quantified reduction of phosphorylated ezrin indicates decreased cortical tension in dr-iRPE, consistent with both our Brillouin measurements and existing literature [87]. Finally, we were surprised to find that many structural and mechanical adaptations are associated mainly with the apicolateral domains. In fact, a direct interplay between the structural and mechanical remodelling of cell–cell and cell–ECM adhesions has been widely reported [88–93]. Except for epithelial buckling during morphogenesis [90] or pathology [94], this homeostatic balance is generally linear: reinforcement and increased tension at intercellular junctions are typically accompanied by enhanced cell–ECM adhesion and increased traction forces [89]. Nevertheless, in our case, no apparent reinforcement has been detected at the basal side of the monolayer. This may be attributed to our study conditions, where iRPE cells are cultured on polyacrylamide hydrogels, which provide strictly controlled physical and biochemical cues with a limited possibility for cell-mediated remodelling. Future studies need to elucidate the contribution of ECM cues and cell-mediated ECM remodelling as part of the puzzle of age-related structural remodelling of the outer retina.

Our work suggests that age-associated structural phenotype goes hand in hand with actomyosin organisation and remodelling capacity, which affects the RPE function of POS fragments internalisation. Phenotypically, we observe an overall higher contractility and shifts in the expression of nucleators and other actin-related proteins. The apical domain of RPE cells requires high remodelling capacity due to its essentiality for the internalisation function [49]. In this study, we observed an apicobasal cell remodelling with bulging and lateral relocalisation of cell-cell junctions during the POS internalisation assay, which has not been reported before. Extensive studies on phagocytosis in macrophages have demonstrated that efficient phagocytic cup formation requires coordinated mechanical remodelling of the plasma membrane and cortical actin [95–97]. In contrast to isolated cells, RPE cells cannot remodel their apical membrane without simultaneously remodelling the interaction with their neighbours, due to their tight epithelial organisation. Therefore, unlike single-cell phagocytosis, phagocytosis in the RPE can be envisioned as a more collective phenomenon, in which neighbouring cells coordinate lateral remodelling to support apical bulging and phagosome formation. The observed phenomena may arise from the synergy of conditions in our culture system, where we observe mature cells of nearly three weeks cultured on soft substrates, as opposed to the majority of other studies, which are being conducted on stiff cell culture plastics or glass substrates. In our model of cell density reduction, we observed a lack of apical bulging and prominent actin-rich protrusions during internalisation. The absence of bulging may stem from the difficulty in disassembling junction-associated structures, which are

more reinforced and stable, or from their connection to highly crosslinked or bundled actin structures. A logical explanation is that increased contractility at the cell-cell junction, necessary to maintain tissue integrity, may redirect actin dynamics from the apical side. This could limit the cytoskeletal and membrane flexibility required for efficient apical processes, including phagosome formation and the development of sufficient tension to engulf POS fragments. The observed formation of large actin-rich protrusions exclusively in dr-iRPE is reminiscent of “arms” structures described in the early embryo [98] and may reflect an altered remodelling capacity, or plasticity, of the membrane-cortex complex. The formation of these protrusions is driven by Arp2/3 activity [98], which is highly versatile both in maintaining junctional integrity [99], regulating cortical thickness and tension [66], as well as playing a major role in the internalisation process [48,52]. Its activity may be diverted towards a new housekeeping maintenance of cortical and junctional actin structure, as opposed to on-demand availability for internalisation. The role of formins in RPE function remains unexplored to date, but our data suggest that they both influence the efficiency of POS phagocytosis and phagocytic cup size when inhibited. This effect may occur through alterations in membrane curvature or surface ruffling, impacting the contact area for internalisation. Notably, inhibition of Myosin II with blebbistatin did not affect the size of internalised POS fragments, but only their number, thereby excluding a role for contractility in regulating phagosome size.

Our findings demonstrate that structural adaptation to cell loss reprogrammes actin organisation, stabilising filaments and redirecting actin towards lateral junctions. This reinforcement limits cytoskeletal responsiveness at the apical surface, constraining the dynamic remodelling required for POS phagocytosis. Thus, the monolayer adopts a new mechanical homeostasis that prioritises structural integrity over functional plasticity. We propose that this stability–flexibility trade-off is a hallmark of postmitotic tissues, offering protection at the expense of specialised functions. This mechanobiological shift provides insight into ageing-related decline in tissues such as the retina and brain [24,25,100–103], and may extend to proliferative epithelia. Future work should determine how density and architecture-driven changes in mechanics contribute to progressive functional loss across tissues.

METHODS

Preparation of cell hydrogel substrates

The surface of 20 mm glass-bottom dishes (Cellvis, D35-20-0-N) or 6-well glass bottom plates (Cellvis, P06-1.5H-N) was activated to allow hydrogel attachment by etching with 0.1 M NaOH (Merck, 106498), followed by reaction with 4% (3-Aminopropyl)triethoxysilane (Sigma Aldrich, 440140) in isopropanol (VWR, 20842) and final incubation with 1% Glutaraldehyde (Merck, 354400) in double distilled water (ddH2O) (B. Braun, 0082479E).

Polyacrylamide hydrogels of 4 kPa stiffness were prepared from an 5%/ 0.1% Acrylamide/Bis-Acrylamide (Bio-Rad 1610140, Bio-Rad 1610142) mixture in ddH2O

by radical polymerisation upon addition of the initiators ammonium persulfate (Sigma Aldrich, 248614) at 0.5% (vol/vol) and N'-Tetramethylethylenediamine (Sigma Aldrich, 411019) at 0.05% (vol/vol), as previously described [104].

Hydrogels were trimmed to size of 4 mm before functionalisation with Laminin-511 (Biolamina, LN511) and Laminin-332 (Biolamina, LN332) at a concentration of 15 µg/ml respectively. Briefly, a functionalisation solution was prepared from ddH2O, 0.5 M HEPES (Carl Roth, 9105) pH 6, 100% ethanol (Sigma Aldrich, 32205) and 0.2% (vol/vol) Bis-Acrylamide. The solution was degassed for 20 min and was completed by adding 0.2% Di(trimethylopropane)tetraacrylate (Sigma Aldrich, 408360), 3% (wt/vol) Hydroxy-4′-(2-hydroxyethoxy)-2-methylpropiophenone (Sigma, 41089 and 0.03% (wt/vol) Acrylic acid N-hydroxysuccinimide ester (Sigma, A8060) as previously described [105]. Hydrogels were dehydrated with 70% ethanol for 5 min, incubated under UV for 10 min with the functionalisation solution and washed with 25 mM HEPES and PBS for a total of 20 min before adding the protein solution. The gels were incubated with the protein solution overnight at 4ºC.

Culture of human induced pluripotent stem-cell derived RPE

HiPSCs-derived RPE cells (Fujifilm Cellular Dynamics, R1102) were seeded in 24-wellplates coated with 2.5 µg/ml vitronectin XF (StemCell Technologies, 07180). Cells were cultured in MEM-alpha with nucleosides (Thermo Fisher, 12571063), supplemented with 1x Glutamax (Thermo Fisher, 35050061), 5% (vol/vol) Knockout Serum replacement (Gibco, 10828028), 1% (vol/vol) N2-Supplement (Gibco, 17502048), 55 nM Hydrocortisone (Sigma Aldrich, H6009), 250 µg/ml Taurine (Sigma Aldrich, T8691), 14 pg/ml Triiodo-L-thyronine (Sigma Aldrich, T5516) and 25 µg/ml gentamycin (Gibco, 15750060) following the manufacturer's instructions. The medium was exchanged every other day. For seeding on hydrogels, cells were detached from the 24-wellplate by 30 min incubation with 5 mM PBS/EDTA (Sigma Aldrich, E6511), followed by 5 min incubation with TrypLE Express (Gibco,126050). Cells were seeded on the UV-sterilized functionalised hydrogels at 5000-6000 cells/mm^2. The medium of cells on hydrogels was exchanged halfway twice a week.

On-demand apoptosis for generation of density-reduced iRPE (dr-iRPE)

Apoptosis was induced by expression and on-demand dimerisation of recombinant FKBP-caspase8 (FKBP-casp8) fusion protein [41]. The FKBP-casp8 containing plasmid was delivered packaged in AAV5 (VectorBuilder, VB230127-1043eaq). Briefly, on day 10 after seeding on the hydrogel, cells were transduced with the virus at 7x10^6 infectious units per cell for 24 h. On day 15, 120 h after the transduction, FKBP-casp8 was dimerised by addition of 100 nM AP20187 in medium (Sigma Aldrich, SML2838) for 24 h. Paired control monolayers were also subjected to the AP20187 treatment. The read-out was performed on day 20, or 96 h after apoptosis treatment finalisation.

Virus, mixed and medium-transfer controls

To exclude effects of the AAV as a delivery system, we used an AAV5-packaged construct that promotes the expression of green fluorescent protein (GFP) (VectorBuilder, VB10000-9287ffw) as a control. Cells were transduced and treated the same way as described for FKBP-casp8 expressing cells, including same timing of viral transduction, AP20187 treatment and read-out.

To obtain a mixed population of transfected and naïve cells, two days prior to seeding on hydrogels, we transduced hiPSCs-derived RPE in a 24-well plate at $7x10^6$ infectious units per cell for 24 h with the FKBP-casp8 vector (VectorBuilder, VB230127-1043eaq). The virus solution was replaced with fresh medium after 24 h. After another 24 h, we seeded a 10%/90% mixture of the transduced hiPSCs-derived RPE cells and naïve hiPSCs-derived RPE on the hydrogels as described above. On day 15, corresponding to the same apoptosis timing of dr-iRPE generation, apoptosis was induced by addition of 100 nM AP20187 (Sigma Aldrich, SML2838) for 24 h. The read-out was performed at 96 h after apoptosis treatment finalisation.

To exclude possible effects of the release of apoptotic debris during the apoptosis, 16 h after AP20187 addition, the medium from dr-iRPE samples was transferred onto control conditions. The medium was then replaced after apoptosis treatment finalisation. 24 h after apoptosis finalisation, the medium from dr-iRPE samples was again transferred to control samples and the samples were maintained in this conditioned medium until read-out.

EdU incorporation-based proliferation assay

Proliferation was assessed by evaluating the incorporation of the base 5-Ethinyl-2'-Desoxyuridin (EdU) with the Click-iT EdU kit (Thermo Fisher, C10337). Cells were incubated with 1:1 mixture of 20 µg/ml EdU and cell culture supernatant for 24 h. The subsequent EdU development reaction was performed following the manufacturer's instructions. Monolayers were imaged completely as overviews of stitched tiles at inverted epi-fluorescent microscope Zeiss Axio Observer 7. Positive cells were identified by using the particle analysis tool in Fiji and their number was normalised to the total number of cells, as detected by DNA labelling by DAPI (1 µg/ml, Invitrogen D1306).

Photoreceptor fragment phagocytosis assay

Photoreceptor outer segment fragments were isolated from porcine eyes obtained from a local slaughterhouse and labelled with FITC (Thermo Fisher, F1906) as previously described [106]. For the assay, the vial was thawed and washed with medium at 2300 g for 5 min. The pellet was resuspended in complete hiPSCs-derived RPE medium together with the bridging molecules human Protein-S (Coachrom, pp012A) at 2 µg/ml and human MGF-8 (R&D Systems, 2767-MF-050) at 2.4 µg/ml. An approximate ratio of ten photoreceptor outer segment fragments per RPE cell seeded was used. Cells were incubated for 4 h, washed four times with DPBS with Ca^{2+} and Mg^{2+} (Gibco, 14040117) and fixed with 2% paraformaldehyde

(Merck, 818715) for 8 min at room temperature (RT). Samples were then permeabilised with 0.3% Triton-X-100 (Sigma Aldrich, T8787) for 2 min and labelled for actin with Phalloidin AF568 (Molecular probes, A12380). Three z-stacks per monolayer were recorded at Zeiss LSM710 Confocal Microscope with ZEN Black software with 40x water immersion objective (ZEISS, 420862-9970-000) in Airyscan super resolution mode. The subsequent analysis was performed in Imaris v10.2.0 (Oxford Instruments).

Nanoindentation and dynamic mechanical analysis

Nanoindentation was performed on a Chiaro Nanoindentor (Optics 11 Life) mounted on an inverted epifluorescence microscope Zeiss Axio Observer 7 with environmental control. Measurements were performed on living cells in displacement control mode using a spherical probe of 20 µm diameter and 0.025 N/m stiffness. Three matrix scans of 16 indentations were recorded per monolayer, indenting 6 µm into the cells. Dynamic mechanical measurements were performed at 1, 2, 4 and 10 Hz to allow for viscoelastic characterisation. For the analysis, indentation portions between the contact point and 2.5 µm were fitted using the Hertz model in the Optics 11 Analysis Software, allowing a range for the contact point fit of 30% of the maximum load. Effective Young's modulus values of fit R^2 better than 0.95 were used for further statistics. Loss and storage moduli were determined for the different frequencies (1 Hz, 2 Hz, 4 Hz and 10 Hz) using the software default methods.

Immunofluorescent labelling and imaging

Monolayers on hydrogels were fixed with 2% paraformaldehyde (Merck, 818715) for 8 min at RT and permeabilised with 0.3% Triton-X-100 (Sigma Aldrich, T8787) for 2 min at RT. Samples were then blocked with 1% BSA (Serva, 11930) in PBS for 30 min at RT, followed by incubation with primary antibodies (Table 1) in blocking solution overnight at 4ºC. After washing, secondary antibodies (Table 1) diluted in PBS were added for 2 h at RT. Samples were washed and mounted in Mowiol mounting medium (Carl Roth, 9002-89-5) before imaging. Unless started otherwise, samples were imaged at Zeiss LSM710 Confocal Microscope with 40x water immersion objective (ZEISS, 420862-9970-000) in Airyscan super resolution mode as z-stacks of 0.5 µm optical slicing. Uniform imaging settings were used between samples within the same experiment. Images were then inspected and further processed for different analyses using Fiji [107].

Bulk RNA sequencing

RNA isolation for RNA sequencing was performed using the RNeasy Micro RNA isolation kit (Qiagen, 74004) with DNase treatment following the manufacturers protocol. Bulk RNA sequencing was performed by the Life & Brain NGS Core Facility (Bonn, Germany) after QuantSeq 3'-mRNA Library Prep/ Lexogen enrichment at NovaSeq 6000 with a depth of 20M reads. The raw data was processed using nf-core/rnaseq v3.12.0 (https://doi.org/10.5281/zenodo.1400710) of the nf-core

collection of workflows [108]. The pipeline was executed with Nextflow v23.04.1 [109]. The complete data set is available on the Gene Expression Omnibus repository (GEO accession number GSE297557). Differential expression analysis was performed using DESeq2 package [110] in R, applying an alpha of 0.05. Genes were considered differentially expressed at an adjusted p-value lower than 0.1. Heatmaps were generated from the DESeq data set after z-normalisation using the package pheatmap [111] and a custom-curated gene list. Functional enrichment of terms related to differentially expressed genes was performed using the g:Profiler online tool [112] using the terms GO molecular function, GO cellular component and GO biological process as well as the pathways KEGG, Reactome and WikiPathways. For comparison, publicly available data on the ageing human RPE was obtained from Butler et al.[55] and Cai et al. [54].

Immunoblotting

Samples were harvested using RIPA buffer [113] with phosphatase inhibitors PhosSTOP™ (Roche, 4906845001) and were subjected to DNA digestion for 15 min by Pierce Universal Nuclease for cell lysis (Thermo Fischer, 88700) prior to addition of Lämmli buffer [114]. Samples were then heated to 95 ºC for 7 min and ca. 10 µg were loaded onto a 10 to 14% (depending on target protein molecular weight) polyacrylamide gel [115] for SDS-PAGE together with a ProSieve Quadcolor Protein Marker (Lonza, 00193837). Proteins were blotted onto Immobilion-P PFDV membrane (Thermo Fischer 88518) and labelled with primary and secondary antibodies for different targets (Table 1). Bands were detected at the Fusion Solo (Vilber Lourmat) after detection with the Pierce™ ECL Western blotting substrate (Thermo Fischer, 32106). The signal was quantified in Fiji [107] by using equal-sized region of interest (ROI) for all bands and measuring the mean grey value. The measurements for the proteins of interest were normalised to the housekeeping protein GAPDH.

Modulation of actin nucleator and myosin II activity

Actin nucleation by Arp2/3 was modulated by using CK-666 (Tocris Bioscience, #3950) at 500 nM in medium. After 1 h incubation, the monolayers were characterised by nanoindentation. For phagocytosis studies, the monolayers were incubated for 30 min with 500 nM CK-666, followed by incubation with the photoreceptor fragments and the bridging molecules in CK-666 containing medium for 4 h. For modulating formin activity, 20 µM SMIFH2 (Tocris Bioscience, #4401) was used instead keeping the same timing and procedure. DMSO at a paired concentration was used as carrier control. For the incubation with different SMIFH2 concentrations, a series of dilutions was prepared starting from a 100 µM solution, resulting in a dilution series of 100, 40, 20 and 5 µM concentrations. For nanoindentation and POS functional studies, the same timing and procedure were used as described above with DMSO as a carrier control. Myosin II inhibition was performed using 5 µM blebbistatin (Abcam, ab120425) for 1 h before nanoindentation and for 30 min before POS addition in blebbistatin-containing medium (see above).

Analysis of extrusion events

Extrusion events were quantified from live cell imaging of apoptosis induction on SiR-Actin (Spirochrome, SC001) labelled cells. The last 15 hours of apoptosis induction were used for the quantification which relies on extrusion events being visible as very bright spots. The video was aligned to correct for stage shifts, smoothed using a Gaussian filter and overlayed in a maximum intensity z-projection in Fiji. The resulting image was thresholded to generate a binary mask and extruded cells were counted using the particle analysis tool in Fiji.

Analysis of cell density

Cell density was quantified from snaps of nuclear staining obtained on epi-fluorescence microscope at 20x magnification. Three to four snaps were used per condition per experiment. Nuclear signal was smoothed using a Gaussian filter, then detected by thresholding. The binary mask was subjected to watersheding and the number of nuclei was counted by using the particle analysis tool in Fiji. Density was calculated by dividing the obtained nuclei count to the area of the field of view. Data originates from at least three independent experiments.

Analysis of cell height

Cell height was determined from super resolution z-stacks of F-actin staining in cross-sectional view. Cells were imaged fixed after mounting in Mowiol, which leads to lower absolute height compared to the height detectable in live-cell imaging. Ten cells per stack were measured with the line tool in three stacks per condition from three independent experiments.

Analysis of cell outline segmentation and shape factor calculation

Cellular outlines from F-actin labelling were segmented using cellpose [116]. The generated regions of interest (ROI) were imported in Fiji and the cell area and perimeter were measured to calculate the dimensionless shape factor [117,118].

Analysis of stress fibres

Cells with stress fibres were manually counted using the multipoint tool in Fiji and normalised to the cell number as calculated after segmentation of cells via cellpose.

Analysis of microvilli length

Microvilli length was characterised from cross-sectional views of ezrin labelling in Fiji. Briefly, at least three cross-sections from at least three stacks per condition from three independent experiments were blurred with a Gaussian blur and a threshold was applied to capture the structure. The resulting masks were selected via the magic wand tool and an eclipse fit was performed. The minor axis was used as an approximate measure of the microvilli length.

Photoreceptor fragment phagocytosis analysis

The photoreceptor fragment phagocytosis was characterised using the Software Imaris v10.2.0 (Oxford Instruments). Briefly, the actin labelling was used to create a surface capturing only the apical actin portion of the monolayer. The average z-position of the surface was determined as a cuff-off height to distinguish internal vs external particles. Separately, photoreceptor fragments were segmented as a surface and the cut-off height was used to distinguish between internalised and external fragments. The count and volume of the fragments of both populations was recorded and used for further analysis.

Quantification of apical actin area

The apical actin area of 300 x 300 pixel field of view was segmented from z-stacks of phalloidin staining during photoreceptor internalisation as a surface in Imaris v10.2.0 (Oxford Instruments). For the region of interest, only a set number of slices including the same upper portion of the cell monolayer were used. The covering area, as internally determined by the software, was then noted.

Quantification of vinculin junctional to cytoplasmic ratio

Junctional signal of vinculin was quantified as a ratio of junctional to cytoplasmic mean grey value in single optical sections. For this, paired F-actin signal was used to segment cell outlines via cellpose as described above. The generated ROIs were imported in Fiji and a custom macro was used to ‘slim-down’ the ROIs, invert the mask, watershed the signal and generate ROIs that encompass the junctional regions around cells. The generated junctional ROIs were used to measure grey value as an average per image. The ‘slimmed-down’ cell ROIs were used to measure the cytoplasmic signal. The average values of junctional and cytoplasmic signals per image were used to generate the junctional to cytoplasmic vinculin measurements.

Quantification of junctional pMLC2

Paired samples from the same experiment were stained with the same antibody solution and imaged with the same imaging settings. In single optical sections at the junctional level, pMLC2 signal was thresholded in Fiji making sure the junctional signal is captured. The mean grey value was measured only within the thresholded region. At least three images were measured per condition per experiment.

Quantification of MRTFA

MRTFA was quantified as nuclear to cytoplasmic ratio of the mean grey value. For this, paired cell nuclei signal (DAPI staining) was segmented via cellpose to generate nuclear ROIs. Nuclear MRTFA was measured as average of the mean grey value of all nuclei ROIs within the image. Cytoplasmic MRTFA was measured after setting nuclear ROIs pixels as zero and thresholding the rest of the image. Then, the mean grey value of the thresholded, non-zero region was measured.

Brillouin microscopy

Brillouin imaging was performed using a commercial setup based on an inverted Nikon Ti-2 Eclipse microscope using a vertically polarised, continuous-wave laser (Cobolt Flamenco, λ = 660 nm, ~ 100 mW) beam with a temperature-tuned air-spaced etalon (LightMachinery) attenuated by 0.6 optical density (OD) filter, resulting in approximately 9 mW incident power at the sample. Light was coupled into a confocal circulator (LightMachinery, HF-13311) and directed to the microscope through a polarising beam splitter and a quarter wave plate (QWP) yielding circularly polarised light. Measurements were performed on a motorised translation stage (Prior Scientific, H117E2NN) using an air objective (Nikon S Plan Fluor 20X NA 0.45), achieving an estimated 0.73 µm lateral and 6.52 µm axial resolution. Brightfield and fluorescence imaging were performed sequentially using a Teledyne sCMOS camera and epi-fluorescence illumination (Nikon D-LEDi).

Backscattered Rayleigh and Brillouin signals were collected with the same objective and routed back through the confocal circulator. The Brillouin signal was acquired using a LightMachinery HyperFine spectrometer (HF-8999-PK-660), equipped with a "pump killer" (PK) module with an air-spaced, pressure-tuned etalon to suppress the elastically scattered Rayleigh light and laser line reflection (~ 60 dB attenuation). Frequency-shifted Brillouin Stokes and anti-Stokes components were directed into the spectrometer, comprised of a virtually imaged phase array (VIPA) and a reflective echelle diffraction grating for spectral dispersion. The cross-dispersed orders were focused onto the CMOS camera sensor (Hamamatsu ORCA-Fusion, C14440-20UP) simultaneously acquiring the full spectrum. The typical acquisition time of a single spectrum is 500 ms, with a spectral resolution < 1 pm.

Spectral data acquisition and raster scanning was facilitated with LightMachinery LabView-based software. The x-y pixel coordinates on the CMOS sensor are converted to wavelength (or frequency) and a Lorentzian fit is applied over each Brillouin peak as described by equation (1).

$$I(\omega) = \frac{I_0}{\pi} \frac{\Gamma \omega_B^2}{(\omega^2 - \omega_B^2)^2 + \Gamma^2 \omega_B^2} \#(1)$$

The final Brillouin shift ω_B and linewidth Γ values for a given spectrum were computed by averaging the corresponding values from the Stokes and anti-Stokes peaks forming a single voxel in the raster scan. Z-scans were acquired as a 3x3 matrix in a step size of 20 µm and z-step of 2 µm, z-range of 80 µm, while apical and basal scans were acquired over the region of 50 x 50 µm with a lateral step size of 1.5 µm. The z-position of apical and basal Brillouin scans within the monolayer was selected based on the appearance of the cells in brightfield and SiR-actin fluorescence images. The scans were limited to 15 minutes to obtain an optimal raster scan resolution while maintaining the cell viability. It should be noted that although the average laser power at sample is within the range used in biological

samples, by comparing brightfield images taken before and after the Brillouin scan, some deformation of the sample was observed. This could have occurred due to the heat of the laser affecting the gel or the cells as the RPE cells' pigmentation contributes to the linear laser light absorption.

Brillouin shift data analysis

For segmentation, the Brillouin shift maps from basal layers were linearly scaled and converted into 8-bit grayscale images, proportionally reflecting the original Brillouin shift values. The grayscale images were segmented using cellpose to identify the individual structures within the images. Following segmentation, two populations were defined: "core", corresponding to segmented regions, and "interstitium", corresponding to areas between them. These modified images were then imported into a custom-written MATLAB script, where appropriate binary masks were created and applied to the original Brillouin shift maps to separate the "core" and the "interstitium". For each raster scan, the mean Brillouin shift and the standard deviation was calculated separately for the two regions. The 3 x 3 raster z-scans resulted in 9 representative z-axis line profiles per region, capturing mechanical transition across the sample. Each profile typically displayed a stiffness change from the hydrogel to the monolayer and then from the monolayer to the surrounding cell media. For each sample, 5 of these scans were obtained.

The Brillouin Shift data was imported into a custom-written MATLAB script to identify the local peaks or, where absent, plateaus in the Brillouin shift profiles (https://github.com/GiedreAstra/Example_E3_zscan_RPE.git). Each line profile was smoothed with a Savitzky-Golay filter, the peak was detected using MATLAB's findpeaks function, with a minimum width imposed to prevent false peak identification. A gradient of the filtered z-line was taken. To refine peak localisation, a Gaussian fit was applied across a range of filtered Brillouin shift values. The fitting range was bound by the z-positions at which the local maximum and the minimum of the derivative of the z-line was within an appropriate range from the previously identified peak. The fitted peak value and position were retrieved. In the case of no peak detection, the code identifies the onset of a drop in the plateau by considering the change in the derivative over a moving average window. The corresponding plateau value was then recorded. The performance of the script was checked for individual z-profiles to exclude outliers.

STATISTICAL ANALYSIS

Statistical analysis was performed using GraphPad Prism on paired averaged values originating from at least three independent biological experiments. Datapoints from at least three technical replicates or from matrix measurements within the samples, epithelial monolayers, were averaged into representative values from a biological replicate. Assuming normal distribution, the data was tested with a paired, two-sided test depending on experimental design with statistical tests and number of biological replicates for each graph given in the captions of the figures.

DECLARATION OF AI USE

The preparation of this manuscript has been aided by AI-assisted technologies to improve its readability and language.

ACKNOWLEDGMENT

We would like to acknowledge all the members of the REMeD group in the past years for their contributions to the discussion of the work. Moreover, we appreciated Adam Breitscheidel's technical support in graphic design, Gloria's excellent help in imaging and insightful feedback from Rudolf Leube. We would like to acknowledge the support of Chris Davis from the Centre for Virus Research of the University of Glasgow for providing a lab space in Garscube campus to enable AAV work needed for the sample preparation for Brillouin microscopy. This work was supported by the Two-Photon Imaging Facility of the Interdisciplinary Center for Clinical Research (IZKF) within the Faculty of Medicine at RWTH Aachen University.

FUNDINGS

This work in Di Russo's laboratory was supported by: A grant from the Interdisciplinary Centre for Clinical Research within the Faculty of Medicine at the RWTH Aachen University and German Research Foundation (DFG; RU 2366/3-1). Furthermore, J.D.R. and W.W. are supported by the DFG within 363055819/GRK2415.

The collaboration with Vassalli's lab for Brillouin microscopy was supported by: RS MacDonald Facility Access funding grant by the Scottish Universities Life Sciences Alliance (SULSA). A travel grant by the German Academic Exchange Service (DAAD) program number 57745342 and a travel grant by Boehringer Ingelheim Fonds.

T.P. and A.N.K. are supported by Add-on Fellowships of the Joachim Herz Foundation.

AUTHORS CONTRIBUTION

JDR conceived and supervised the project. TP designed and performed all the experiments. GA, ANK and TP performed Brillouin measurements. GA and ANK performed Brillouin analysis. MM performed initial transcriptomics data analysis and advised on the transcriptomic exploration. RR supported the immunoblotting experiments. SS supported with confocal imaging. LY supported the establishment of viral transduction. WW and MV supported the work with expertise and advice. JDR and TP wrote the manuscript, and all authors discussed and commented on it.

COMPETING INTERESTS

Authors declare that they have no competing interests.

DATA AND MATERIALS AVAILABILITY

All data are available in the main text or the supplementary materials. Furthermore, the complete data set of RNA bulk sequencing is available on the Gene Expression Omnibus repository (GEO accession number GSE297557).

Supplementary figures

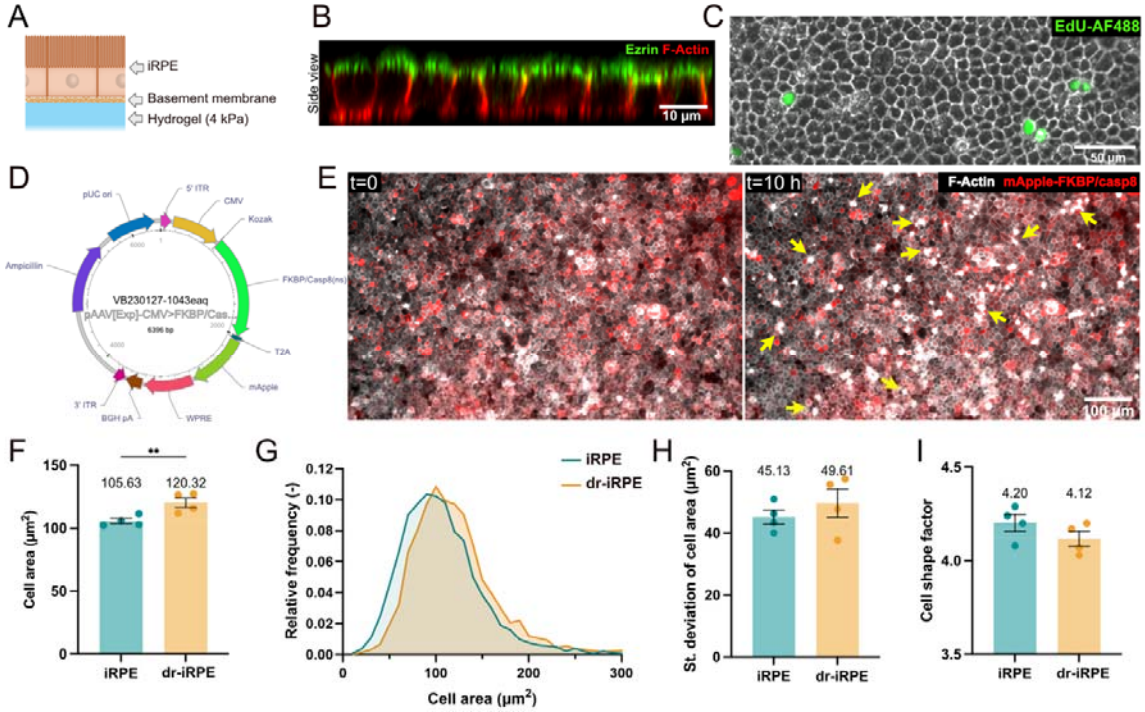

Suppl. figure 1: The iRPE and dr-iRPE model and cell morphometric characterisation. A: Schematics of iRPE cell culture system displaying the monolayer obtained on 4 kPa hydrogels functionalised with basement membrane mimicking coating. **B:** Cross-section of iRPE after 20 days of culture labelled for F-actin (red) and ezrin (green) showing characteristic apicobasal polarisation. **C:** Representative micrograph of proliferation assay showing iRPE cells in brightfield and proliferating cell nuclei labelled by EdU-AF488 (green). **D:** Map of plasmid used for the expression of pro-apoptotic FKBP-casp8 protein and delivered to iRPE cells by AAV5. **E:** Representative micrographs of SiR-actin labelled iRPE (white) expressing mApple as fluorescent reporter (red) at the timepoint of AP20187 addition and 10 h afterwards. Extrusion events of apoptotic cells at the latter point are indicated with yellow arrows. **F:** Quantification of average cell area (n=4). **G:** Relative frequency distribution of cell areas (from 3263 (iRPE) and 2821 (dr-iRPE) cells from n=4). **H:** Standard deviation of cell areas within an experiment (n=4). **I:** Average cell shape factor (n=4). Datapoints represent average values ± SEM per experiment. Statistical significance was tested using a paired t-test, where **: $p<0.01$.

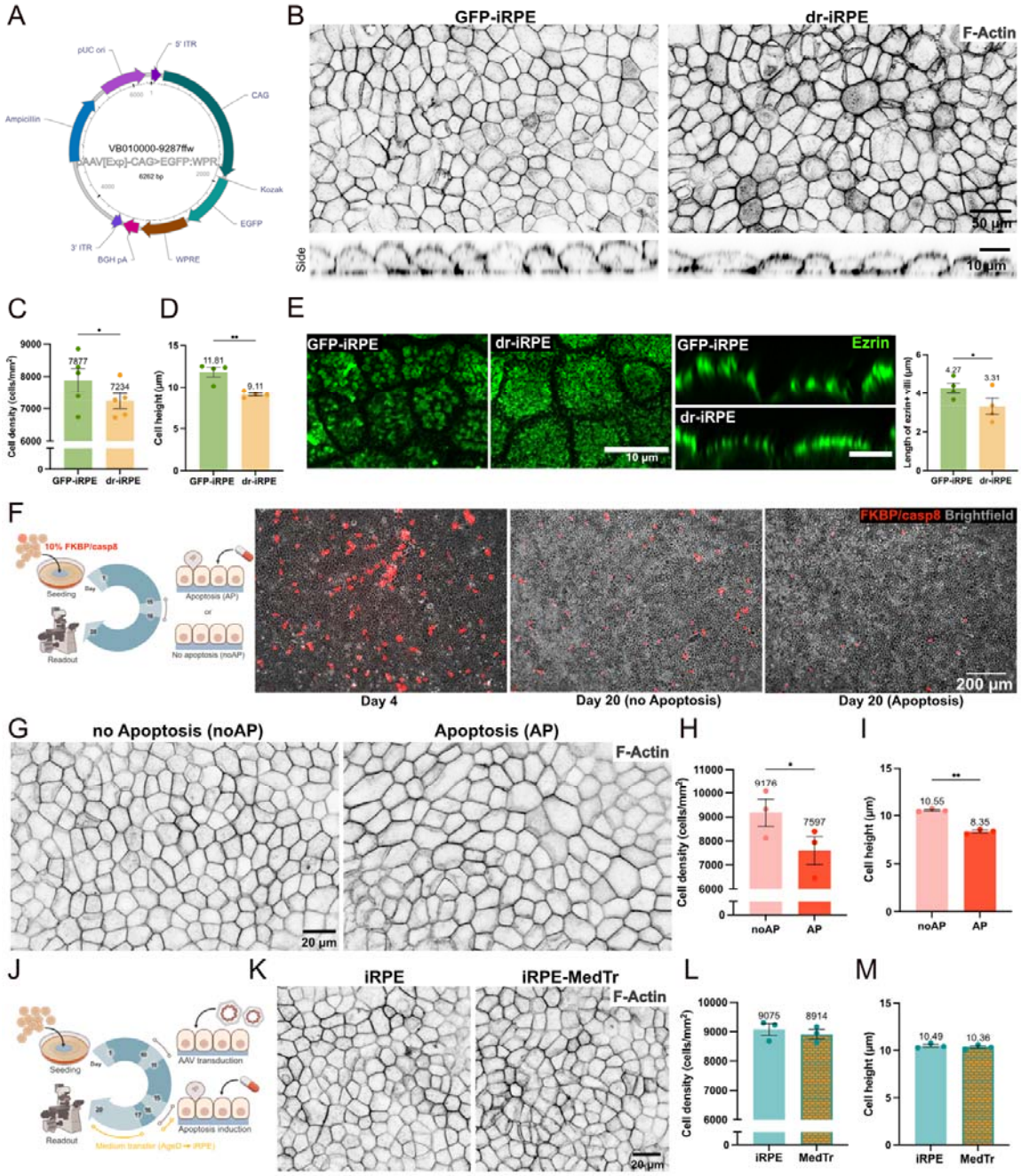

Suppl. figure 2: Controls for influence of virus, recombinant FKBP-casp8 protein expression and debris released into medium. A: Vector map of plasmid used as viral control, which promotes the expression of GFP. **B:** Representative micrographs of F-actin in GFP-iRPE compared to dr-iRPE (top) and cross sections (down). **C:** Quantification of average cell density for GFP-iRPE (n=5). **D:** Quantification of cell height for GFP-iRPE (n=4). **E:** Representative micrographs showing ezrin as maximum intensity projection in top (left) and side views (middle) and the quantification of ezrin-positive microvilli length (right, n=4). **F:** Experimental schematics of mixed population control. The micrographs show representative monolayers of mApple-positive transduced cells within the naïve cells at day 4 and at day 20 (the readout day). **G:** Representative micrographs of F-actin labelled mixed population iRPE without apoptosis induction (noAP) and after induction of apoptosis (AP). **H:** Quantification of average cell density for the mixed population control (n=3). **I:** Quantification of cell height for the mixed population control (n=3). **J:** Experimental schematics of medium-transfer control **K:** Representative micrographs of F-actin labelled control monolayers vs. monolayers subjected to medium transfer. **L:** Quantification of average cell density for the medium transfer control (n=3). **M:** Quantification of cell height for the medium transfer control (n=3). Datapoints represent average values per experiment ± SEM. Statistical significance was tested using a paired t-test, where *: p<0.05, **: p<0.01.

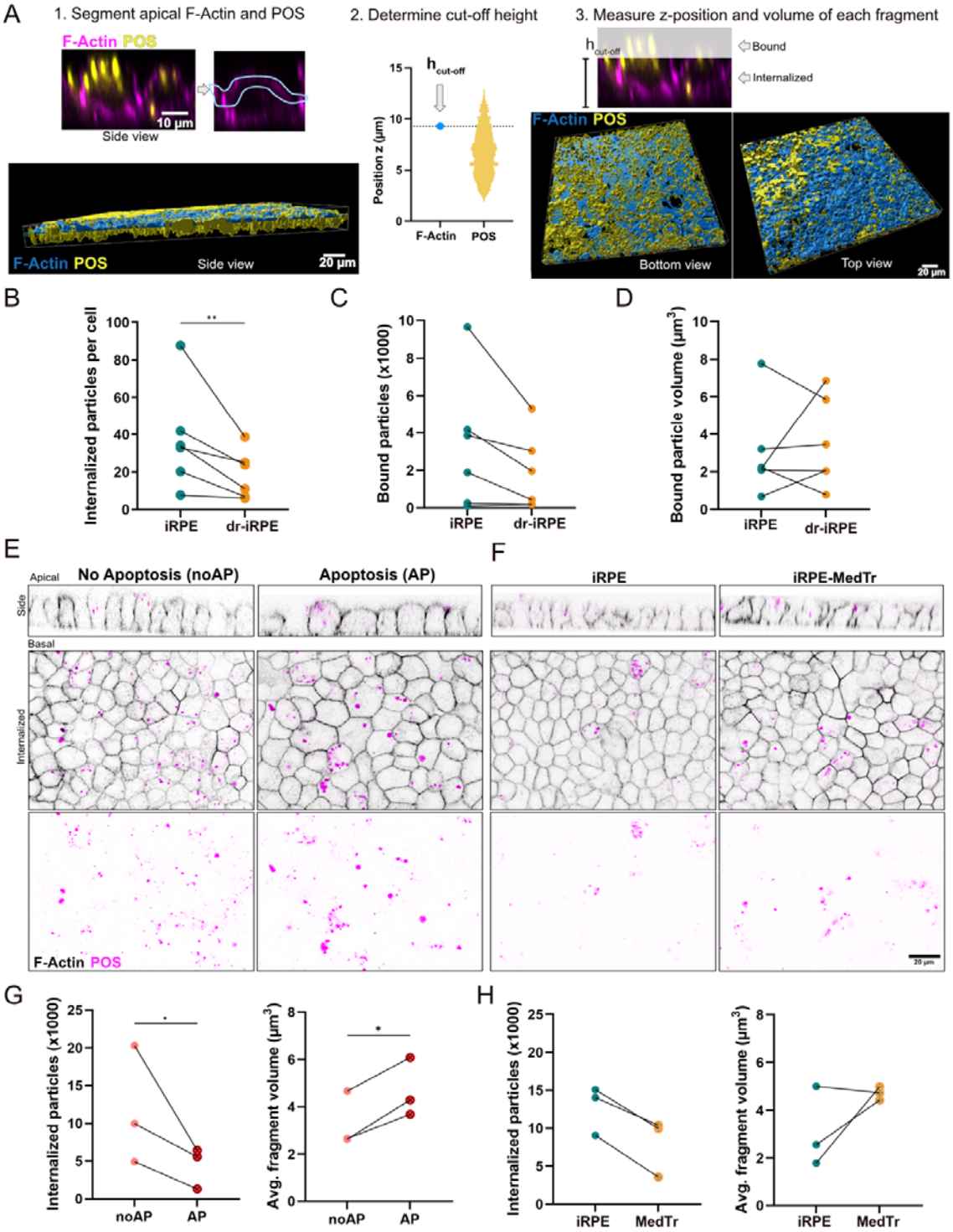

Suppl. figure 3: POS internalisation assay. A: Workflow for 3D segmentation, cut-off height determination and classification into 'bound' vs 'internalised' particles. **B:** Quantification of number of internalised POS particles normalised to cell number (n=6). **C:** Quantification of bound POS particles number in the field of view (n=6). **D**: Quantification of average bound POS particle volume (n=6). **E:** Representative micrographs of iRPE at t = 4 h of POS internalisation assay as orthogonal cross-sections (up) or as single optical slices in the middle of cells (lower two panels) for the "mixed" control. **F:** Representative micrographs of iRPE at t = 4 h of POS internalisation assay as orthogonal cross-sections (up) or as single optical slices in the middle of cells (lower two panels) for the medium-transfer control (MedTr). **G:** Quantification of POS fragments internalised within the time of the assay per

field of view (left) and quantification of the average volume of internalised fragments (right) for the “mixed” population control (n=3). **H:** Quantification of POS fragments internalised within the time of the assay per field of view (left) and quantification of the average volume of internalised fragments (right) for the medium-transfer control (n=3). Datapoints represent average values per experiment. Statistical significance was tested using a paired t-test, where *: p<0.05, **: p<0.01.

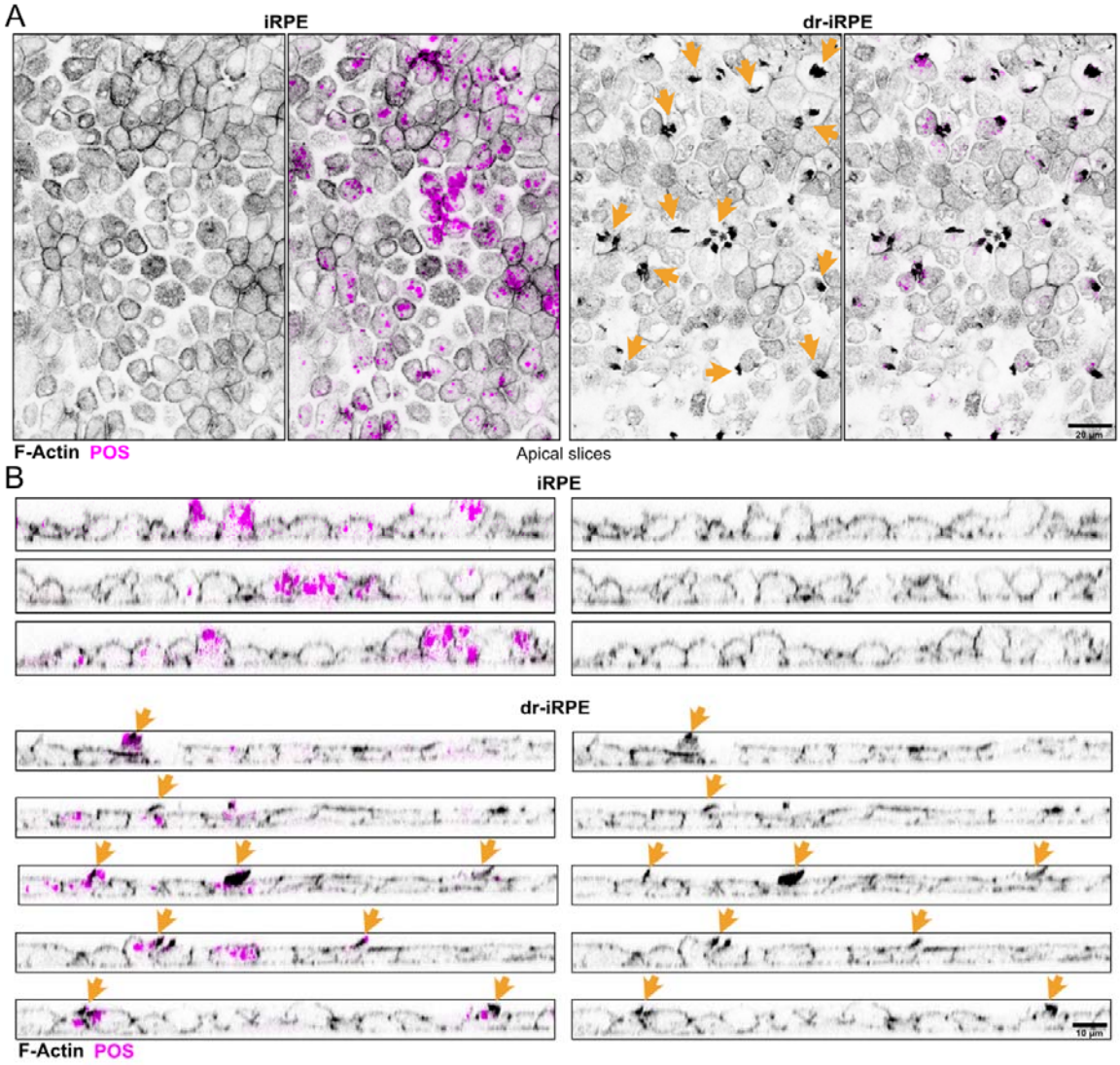

Suppl. figure 4: Differential apical actomyosin remodelling between iRPE and dr-iRPE during POS internalisation assay. A: Representative micrographs of the apical side of monolayers during internalisation showing F-actin and photoreceptors. Arrows point to the presence of protruding actin-rich structures in dr-iRPE. **B:** Representative orthogonal cross sections of iRPE and dr-iRPE monolayers during internalisation showing F-actin and FITC-labelled POS. Arrows point to actin-rich structures.

A

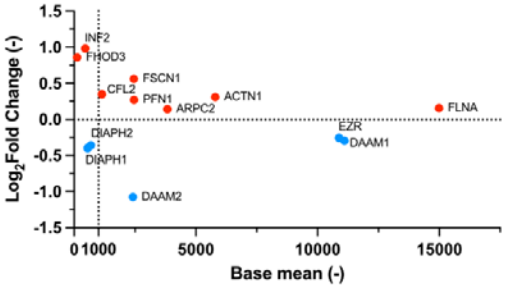

B

Overlapping DEGs with reported age-related changes in humans

Gene symbol	Protein name	Direction change
Cai H. et al. 2012 (DOI:10.3389/fnagi.2012.00008)		
DKK1	dickkopf WNT signaling pathway inhibitor 1(DKK1)	up
LAMA3	laminin subunit alpha 3(LAMA3)	up
TYMS	thymidylate synthetase(TYMS)	up
PLEKHG4	pleckstrin homology and RhoGEF domain containing G4(PLEKHG4)	down
SCN2B	sodium voltage-gated channel beta subunit 2(SCN2B)	down
Butler J. M. et al. 2021 (DOI: 10.1111/jcmm.16569)		
AKAP6	A-kinase anchoring protein 6(AKAP6)	up
BMP8B	bone morphogenetic protein 8b(BMP8B)	up
CCDC51	coiled-coil domain containing 51(CCDC51)	up
CTSV	cathepsin V(CTSV)	up
DUSP6	dual specificity phosphatase 6(DUSP6)	up
KL	klotho(KL)	up
SLC6A20	solute carrier family 6 member 20(SLC6A20)	up
TNFRSF10C	TNF receptor superfamily member 10c(TNFRSF10C)	up
TRPV4	transient receptor potential cation channel subfamily V member 4(TRPV4)	up
CPAMD8	C3 and PZP like alpha-2-macroglobulin domain containing 8(CPAMD8)	down
CSRP2	cysteine and glycine rich protein 2(CSRP2)	down
DCT	dopachrome tautomerase(DCT)	down
GAS1	growth arrest specific 1(GAS1)	down
TMEM150C	transmembrane protein 150C (TMEM150C)	down

C

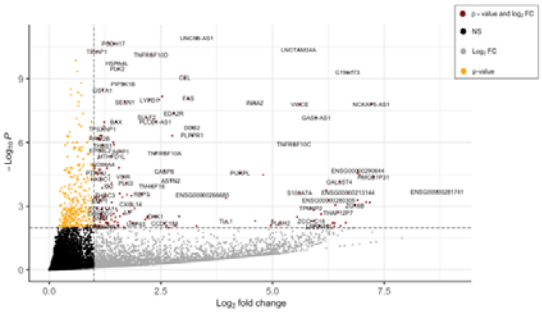

D

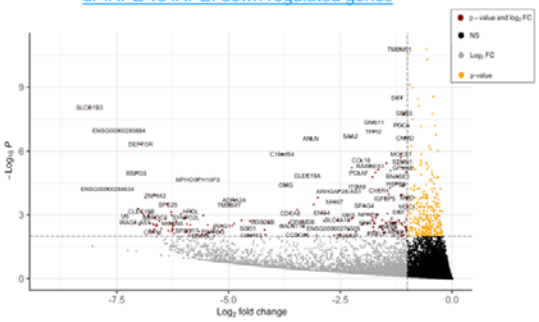

Suppl. figure 5: Density reduced iRPE shows a differential gene expression from iRPE, which is partly overlapping with ageing patients. A: Base mean vs Log2Fold change for significantly differentially expressed actin-associated genes in dr-iRPE vs iRPE (n=4). **B:** Differentially expressed genes (DEGs) overlapping with the results from studies on ageing human RPE from Cai H. et al. [54] and Butler J. M. et al. [55]. Gene names are labelled in blue or red for downregulated or upregulated, respectively. **C:** Volcano plot of upregulated DEGs between dr-iRPE and iRPE. **D:** Volcano plot of downregulated DEGs between dr-iRPE and iRPE. Cut-off lines were drawn at log2fold=1, corresponding to a fold change of two, and at log10P = -2, corresponding to a p of 0.001 and padj of 0.1, which we set as cut-off significance value for DEGs. Genes are assigned to groups based on their log2fold and log10fold values as highlighted in the legend.

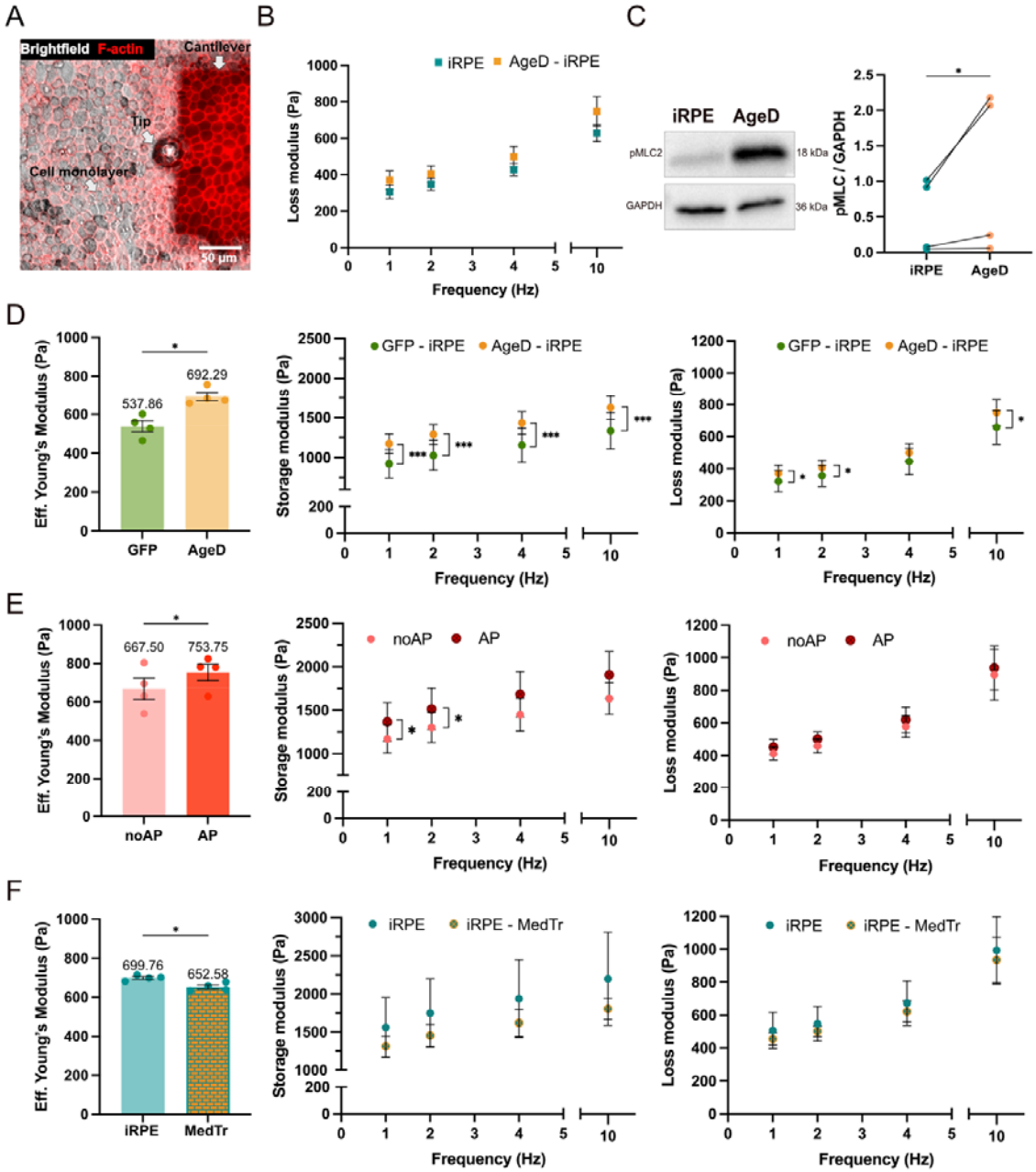

Suppl. figure 6: Biomechanical characterisation of iRPE conditions. A: Experimental setup for performing nanoindentation. The micrograph shows a top view of SiR-actin labelled cell monolayer and cantilever with tip. **B:** Average loss modulus of iRPE and dr-iRPE (n=4). **C:** Immunoblot of pMLC2 and GAPDH as a housekeeping protein and quantification of total pMLC2 protein from immunoblots, normalised to GAPDH (n=4). **D:** Average Effective Young's modulus, storage and loss moduli for virus control (n=4). **E:** Average Effective Young's modulus, storage and loss moduli for treated (noAP) and untreated (AP) mixed population iRPE (n=4). **F:** Average Effective Young's modulus, storage and loss moduli for iRPE and conditioned medium treated iRPE (MedTr-iRPE) (n=4). Datapoints represent average values ± SEM per experiment. Statistical significance was tested using a paired t-test, where *: $p<0.05$ and ***: $p<0.001$.

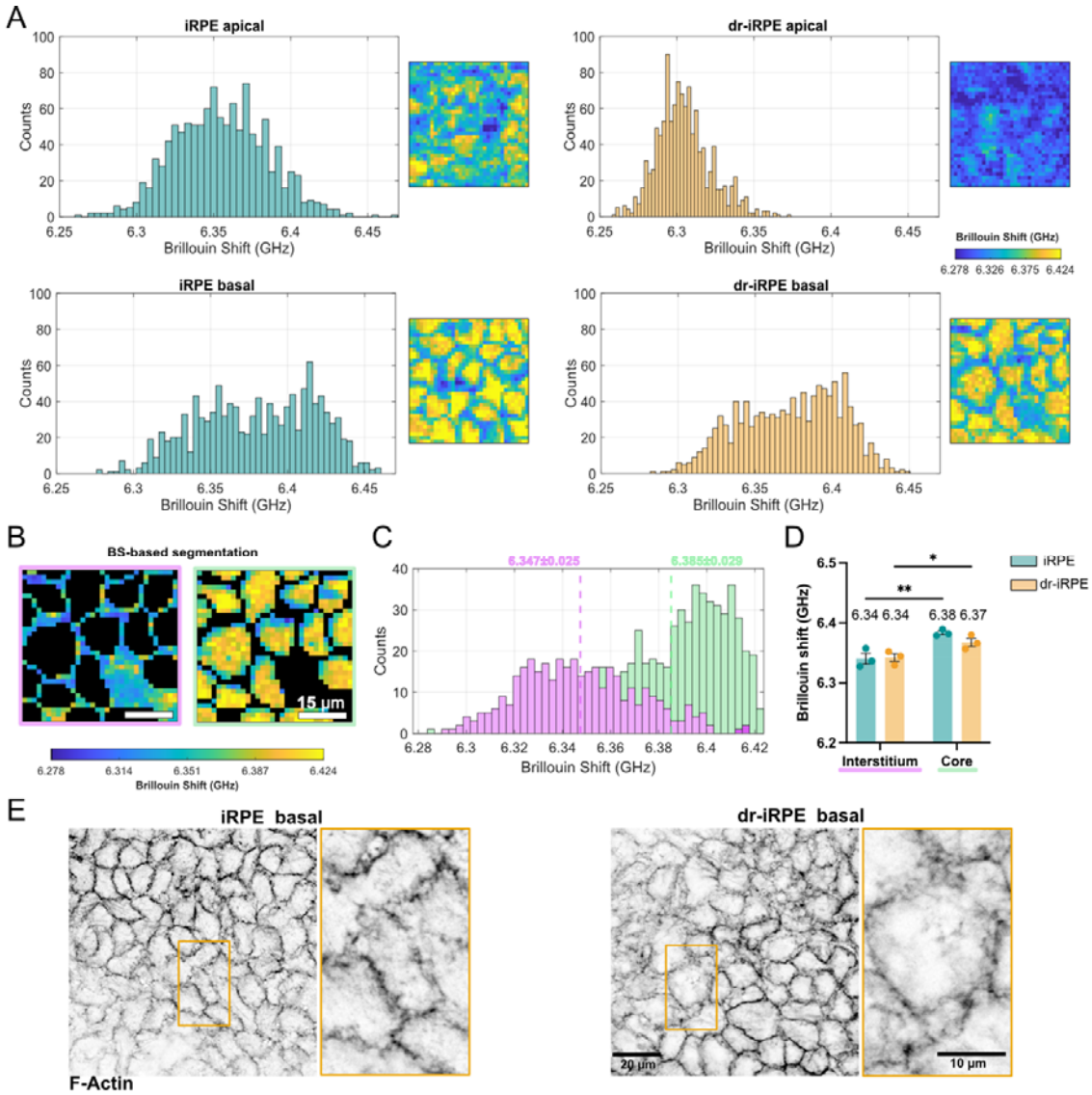

Suppl. figure 7: Distribution of Brillouin shift values in apical and basal layers of iRPE and density reduced iRPE and segmentation of Brillouin shift values from basal maps. A: Representative histograms of iRPE and dr-iRPE basal and apical Brillouin shift values acquired from 50 x 50 µm regions of interest and the respective plots. **B:** Representative plots of segmented Brillouin shift maps from basal scans with two population modes defined by Cellpose segmentation (see Methods). **C:** Representative histogram of the plots shown in B illustrating the identified populations. **D:** Quantification of Brillouin shift population modes named as "Interstitium" and "Core" in basal iRPE and dr-iRPE monolayers (n=3). **E:** Representative F-Actin micrographs of basal iRPE and dr-iRPE monolayers with annotated regions enlarged. Datapoints in D represent average values per experiment ± SEM. Statistical significance was tested using a one-way ANOVA, where *: $p<0.05$ and **: $p<0.01$.

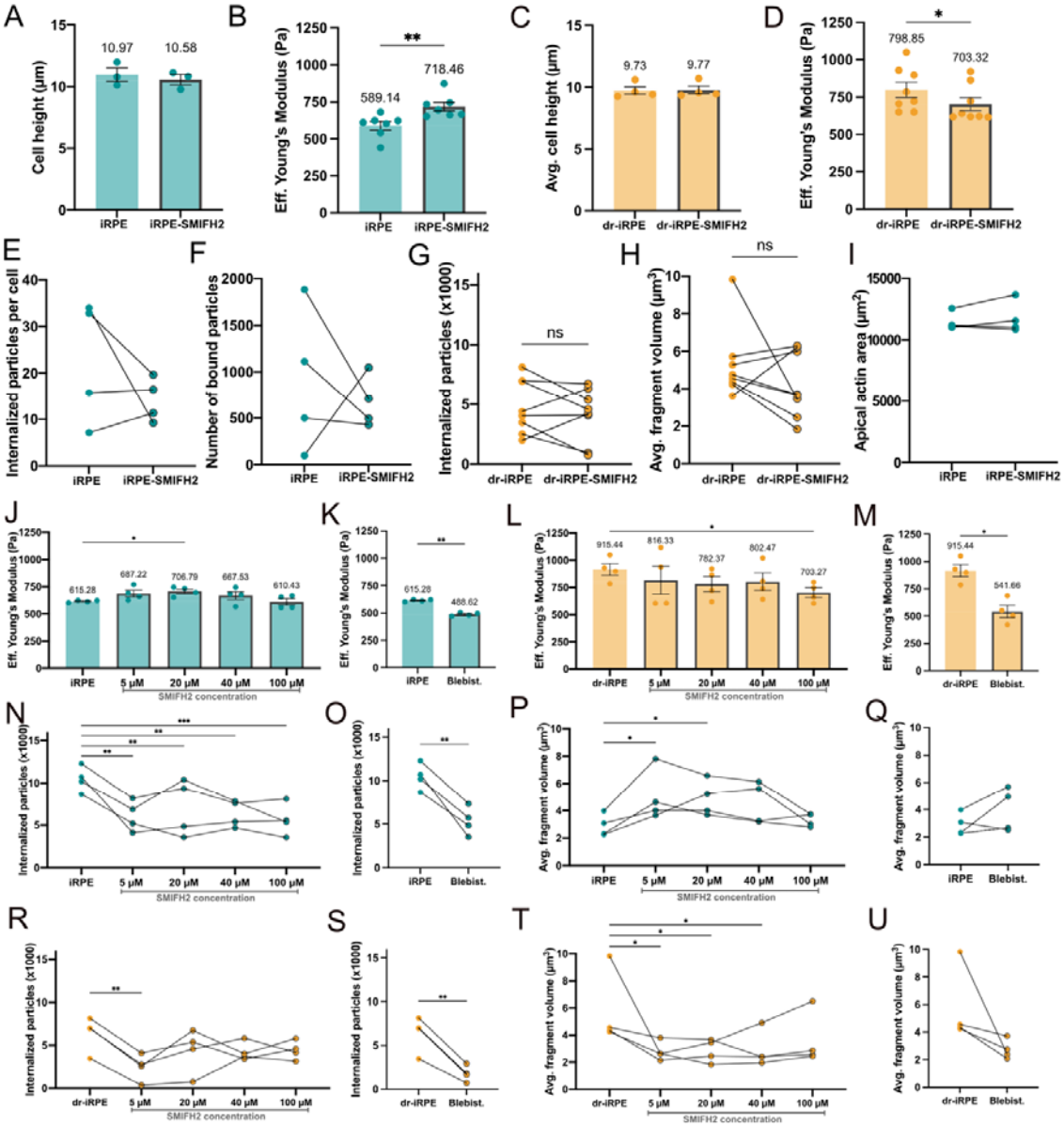

Suppl. figure 8: Linear nucleator inhibition with SMIFH2 during photoreceptor phagocytosis. A: Quantification of cell height for iRPE vs SMIFH2-treated iRPE (n=3). **B:** Average Effective Young's Modulus, derived from 2.5 µm nanoindentation with a 20 µm spherical tip for iRPE vs SMIFH2-treated iRPE monolayers (n=8). **C:** Quantification of cell height for dr-iRPE vs SMIFH2-treated dr-iRPE (n=4). **D:** Average Effective Young's Modulus for dr-iRPE vs SMIFH2-treated dr-iRPE monolayers (n=8). **E:** Quantification of the number of internalised photoreceptor particles normalised to cell number for iRPE vs SMIFH2-treated iRPE (n=4). **F:** Quantification of the number of bound particles in the field of view for iRPE vs SMIFH2-treated iRPE (n=4). **G:** Quantification of the number of internalised photoreceptor particles for dr-iRPE vs SMIFH2-treated dr-iRPE (n=8). **H:** Quantification of the average volume of internalised photoreceptor particles for dr-iRPE vs SMIFH2-treated dr-iRPE (n=8). **I:** Quantification of apical actin area per field of view during internalisation in iRPE vs SMIFH2-treated iRPE (n=4). **J:** Average Effective Young's Modulus of iRPE monolayers after 1 h treatment with SMIFH2 concentrations of 5, 20, 40 or 100 µM (n=4). **K:** Average Effective Young's Modulus of iRPE monolayers after 1 h treatment with 5 µM blebbistatin (n=4). **L:** Average Effective Young's Modulus of dr-iRPE monolayers after 1 h treatment with SMIFH2 concentrations of 5, 20, 40 or 100 µM (n=4). **M:** Average Effective Young's Modulus of dr-iRPE monolayers after 1 h treatment with 5 µM blebbistatin (n=4). **N:** Number of internalized POS particles of iRPE monolayers after treatment with SMIFH2 concentrations of 5, 20, 40 or 100 µM (n=4). **O:** Number of internalized POS particles of iRPE monolayers after treatment with 5 µM blebbistatin (n=4). **P:** Average volume of

internalized particles of iRPE monolayers after treatment with SMIFH2 concentrations of 5, 20, 40 or 100 µM (n=4). **Q:** Average volume of internalized particles of iRPE monolayers after treatment with 5 µM blebbistatin (n=4). **R:** Number of internalized POS particles of dr-iRPE monolayers after treatment with SMIFH2 concentrations of 5, 20, 40 or 100 µM (n=4). **S:** Number of internalized POS particles of dr-iRPE monolayers after treatment with 5 µM blebbistatin (n=4). **T:** Average volume of internalized particles of dr-iRPE monolayers after treatment with SMIFH2 concentrations of 5, 20, 40 or 100 µM (n=4). **U:** Average volume of internalized particles of dr-iRPE monolayers after treatment with 5 µM blebbistatin. Datapoints represent average values (± SEM in case of bar graphs) per experiment. Statistical significance in A, B, C, D, I, K and M was tested using a paired t-test, where *: $p<0.05$ and **: $p<0.01$. Statistical significance in E, F, G, H, O, Q, S and U was tested using a ratio paired t-test, where **: $p<0.01$. Statistical significance in J, L, N, P, R and T was tested using a One-way ANOVA with multiple comparisons, where *: $p<0.05$ and **: $p<0.01$.

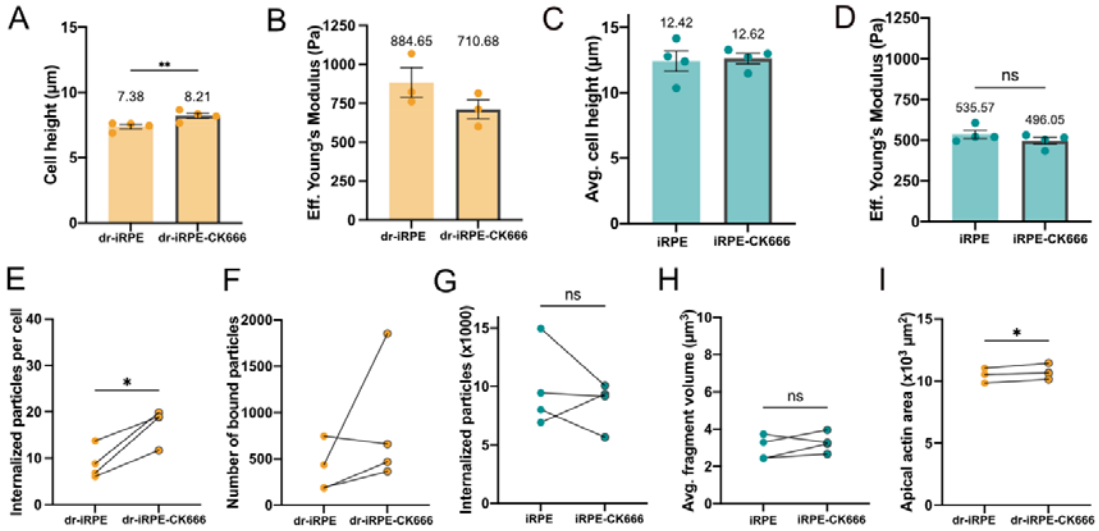

Suppl. figure 9: Branched nucleator inhibition with CK666 during photoreceptor phagocytosis. A: Quantification of cell height for dr-iRPE vs CK666-treated dr-iRPE (n=4). **B:** Average Effective Young's Modulus, derived from 2.5 µm nanoindentation with a 20 µm spherical tip for dr-iRPE vs CK666-treated dr-iRPE (n=3). **C:** Quantification of cell height for iRPE vs CK666-treated iRPE (n=4). **D:** Average Effective Young's Modulus, derived from 2.5 µm nanoindentation with a 20 µm spherical tip for iRPE vs CK666-treated iRPE (n=4). **E:** Quantification of the number of internalised photoreceptor particles normalised to cell number for dr-iRPE vs CK666-treated dr-iRPE monolayers (n=4). **F:** Quantification of the number of bound particles in the field of view for dr-iRPE vs CK666-treated dr-iRPE (n=4). **G:** Number of internalized POS particles of iRPE vs CK666-treated iRPE (n=4). **H:** Average volume of internalized particles of iRPE vs CK666-treated iRPE (n=4). **I:** Quantification of apical actin area per field of view of monolayers during internalisation in dr-iRPE vs CK666-treated dr-iRPE (n=3). Datapoints represent average values (± SEM in case of bar graphs) per experiment. Statistical significance in A - D and I was tested using a paired t-test, where *: $p<0.05$ and **: $p<0.01$. Statistical significance in E - H and I was tested using a ratio paired t-test, where *: $p<0.05$.

Supplementary information

Table 1: Antibodies and dyes used for immunofluorescence (IF) or immunoblotting (WB).

Name	Source	Concentration/Dilution
	Primary antibodies	
Anti phospho-myosin light chain 2 (Ser19)	Cell Signalling, 3671	1:50 (IF); 1:1000 (WB)
Anti vinculin	Sigma, V4139	15 µg/ml (IF)
Anti ezrin	abcam, ab4069	10 µg/ml (IF); 1 µg/ml (WB)
Anti phospho ezrin (Thr567)	Invitrogen, PA5-37763	5 µg/ml (IF); 1 µg/ml (WB)
Anti non muscle myosin heavy chain IIB	BioLegend, 909901	4 µg/ml (IF)
	Secondary antibodies	
AF488 anti mouse IgG (H+L)	Invitrogen, A11001	8 µg/ml (IF)
AF594 anti mouse IgG (H+L)	Invitrogen, A11005	8 µg/ml (IF)
AF594 anti rabbit IgG (H+L)	Invitrogen, A11012	8 µg/ml (IF)
AF647 anti rabbit IgG (H+L)	Jackson/Dianova, 111-605-144	7,5 µg/ml (IF)
AF 488 anti rabbit IgG (H+L)	Jackson/Dianova, 711-546-152	8 µg/ml (IF)
HRP anti rabbit IgG	Abcam, ab99696	1:5000 (WB)
HRP anti mouse IgG (H+L)	Jackson/Dianova, 115-035-003	1:5000 (WB)
	Fluorescent dyes	
Phalloidin-iFluor 488	Abcam, ab176753	1:200 (IF)
Phalloidin-iFluor 647	Abcam, ab176759	1:200 (IF)
Phalloidin AF568	Molecular probes, A12380	1:200 (IF)

Videos Legends

Video 1: On-demand activation of FKBP/casp8 by AP20187 leads to monolayer-scale extrusion events. Live-iRPE monolayer time-lapse expressing FKBP/casp8 (mApple-positive red cells) and labelled with actin dye SiR-Actin (white). Upon the addition of the AP20187 compound, cells are extruded due to apoptosis induction. Extrusion events include neighbouring cells adopting a characteristic rosette-like morphology, while the dying cell is extruded out of the monolayer, forming a bright blob.

Video 2: Live-cell time-lapse of iRPE monolayer during nanoindentation. The SiR-Actin labelled iRPE monolayer is probed by nanoindentation in a matrix scan (left). A zoom-in view (right) reveals the junctional deformation occurring during the measurement.

References

1. Thomson, J. A. On Growth and Form. **100**, 21–22 (1917).

2. Ball, P. *Shapes: Nature's Patterns*. (Oxford University Press, USA, 2009).

3. Bepler, T. & Berger, B. Learning the protein language: Evolution, structure, and function. *Cell Syst.* **12**, 654-669.e3 (2021).

4. Gligorijević, V. *et al.* Structure-based protein function prediction using graph convolutional networks. *Nat. Commun.* **12**, 3168 (2020).

5. Yang, J., Griffin, A., Qiang, Z. & Ren, J. Organelle-targeted therapies: a comprehensive review on system design for enabling precision oncology. *Signal Transduct. Target. Ther.* **7**, 379 (2022).

6. Glancy, B., Kim, Y., Katti, P. & Willingham, T. B. The Functional Impact of Mitochondrial Structure Across Subcellular Scales. *Front. Physiol.* **11**, 541040 (2020).

7. Morgan, E. F. & Gerstenfeld, L. C. Marcus and Feldman's Osteoporosis. 15–35 (2021) doi:10.1016/b978-0-12-813073-5.00002-2.

8. Baum, G. L. *et al.* Development of structure–function coupling in human brain networks during youth. *Proc. Natl. Acad. Sci.* **117**, 771–778 (2020).

9. Simpson, C. L., Patel, D. M. & Green, K. J. Deconstructing the skin: cytoarchitectural determinants of epidermal morphogenesis. *Nat. Rev. Mol. Cell Biol.* **12**, 565–580 (2011).

10. Anlaş, A. A. & Nelson, C. M. Tissue mechanics regulates form, function, and dysfunction. *Curr. Opin. Cell Biol.* **54**, 98–105 (2018).

11. Ayad, N. M. E., Kaushik, S. & Weaver, V. M. Tissue mechanics, an important regulator of development and disease. *Philosophical Transactions Royal Soc B* **374**, 20180215 (2019).

12. Guillot, C. & Lecuit, T. Mechanics of Epithelial Tissue Homeostasis and Morphogenesis. *Science* **340**, 1185–1189 (2013).

13. Biggs, L. C., Kim, C. S., Miroshnikova, Y. A. & Wickström, S. A. Mechanical Forces in the Skin: Roles in Tissue Architecture, Stability, and Function. *J. Investig. Dermatol.* **140**, 284–290 (2020).

14. Guimarães, C. F., Gasperini, L., Marques, A. P. & Reis, R. L. The stiffness of living tissues and its implications for tissue engineering. *Nat. Rev. Mater.* **5**, 351–370 (2020).

15. Gómez-Gálvez, P., Anbari, S., Escudero, L. M. & Buceta, J. Mechanics and self-organization in tissue development. *Semin. Cell Dev. Biol.* **120**, 147–159 (2021).

16. Hannezo, E. & Heisenberg, C.-P. Mechanochemical Feedback Loops in Development and Disease. *Cell* **178**, 12–25 (2019).

17. Kaliman, S. *et al.* Mechanical Regulation of Epithelial Tissue Homeostasis. *Phys Rev X* **11**, 031029 (2021).

18. DuFort, C. C., Paszek, M. J. & Weaver, V. M. Balancing forces: architectural control of mechanotransduction. *Nat Rev Mol Cell Bio* **12**, 308–319 (2011).

19. Ishikawa, J. *et al.* Mechanical homeostasis of liver sinusoid is involved in the initiation and termination of liver regeneration. *Commun. Biol.* **4**, 409 (2021).

20. Eichinger, J. F. *et al.* Mechanical homeostasis in tissue equivalents: a review. *Biomech. Model. Mechanobiol.* **20**, 833–850 (2021).

21. Kozyrina, A. N. *et al.* Laminin-defined mechanical status modulates retinal pigment epithelium phagocytosis. *EMBO Rep.* 1–27 (2025) doi:10.1038/s44319-025-00475-9.

22. Tamori, Y. & Deng, W.-M. Tissue Repair through Cell Competition and Compensatory Cellular Hypertrophy in Postmitotic Epithelia. *Dev. Cell* **25**, 350–363 (2013).

23. Campello, L. *et al.* Aging of the Retina: Molecular and Metabolic Turbulences and Potential Interventions. *Annu Rev Vis Sc* **7**, 1–32 (2021).

24. Terry, R. D., DeTeresa, R. & Hansen, L. A. Neocortical cell counts in normal human adult aging. *Ann. Neurol.* **21**, 530–539 (1987).

25. Freeman, S. H. *et al.* Preservation of Neuronal Number Despite Age-Related Cortical Brain Atrophy in Elderly Subjects Without Alzheimer Disease. *J. Neuropathol. Exp. Neurol.* **67**, 1205–1212 (2008).

26. Piskova, T., Kozyrina, A. N. & Di Russo, J. Mechanobiological implications of age-related remodelling in the outer retina. *Biomater. Adv.* **147**, 213343 (2023).

27. Sparrrow, J. R., Hicks, D. & Hamel, C. P. The Retinal Pigment Epithelium in Health and Disease. *Curr. Mol. Med.* **10**, 802–823 (2010).

28. Panda-Jonas, S., JONAS, J. B. & JAKOBCZYK-ZMIJA, M. Retinal Pigment Epithelial Cell Count, Distribution, and Correlations in Normal Human Eyes. *Am. J. Ophthalmol.* **121**, 181–189 (1996).

29. Bhatia, S. K. *et al.* Analysis of RPE morphometry in human eyes. *Mol Vis* **22**, 898–916 (2016).

30. Priore, L. V. D., Kuo, Y.-H. & Tezel, T. H. Age-related changes in human RPE cell density and apoptosis proportion in situ. *Invest Ophth Vis Sci* **43**, 3312–8 (2002).

31. Katz, M. L. & Robison, W. G. Age-related changes in the retinal pigment epithelium of pigmented rats. *Exp Eye Res* **38**, 137–151 (1984).

32. Ortolan, D. *et al.* Single-cell–resolution map of human retinal pigment epithelium helps discover subpopulations with differential disease sensitivity. *Proc. Natl. Acad. Sci.* **119**, e2117553119 (2022).

33. Tarau, I.-S., Berlin, A., Curcio, C. A. & Ach, T. The Cytoskeleton of the Retinal Pigment Epithelium: from Normal Aging to Age-Related Macular Degeneration. *Int J Mol Sci* **20**, 3578 (2019).

34. Lai, Y. L. & Rana, M. W. A Study of Photoreceptor–Retinal Pigment Epithelium Complex: Age-Related Changes in Monkeys. *P Soc Exp Biol Med* **181**, 371–381 (1986).

35. Inana, G. *et al.* RPE phagocytic function declines in age-related macular degeneration and is rescued by human umbilical tissue derived cells. *J Transl Med* **16**, 63 (2018).

36. Ma, J. Y. W. *et al.* Aging induces cell loss and a decline in phagosome processing in the mouse retinal pigment epithelium. *Neurobiol. Aging* **128**, 1–16 (2023).

37. Brandl, C. *et al.* In-Depth Characterisation of Retinal Pigment Epithelium (RPE) Cells Derived from Human Induced Pluripotent Stem Cells (hiPSC). *NeuroMolecular Med.* **16**, 551–564 (2014).

38. Miyagishima, K. J. *et al.* In Pursuit of Authenticity: Induced Pluripotent Stem Cell-Derived Retinal Pigment Epithelium for Clinical Applications. *STEM CELLS Transl. Med.* **5**, 1562–1574 (2016).

39. Song, M. J. *et al.* Bioprinted 3D outer retina barrier uncovers RPE-dependent choroidal phenotype in advanced macular degeneration. *Nat. Methods* **20**, 149–161 (2023).

40. Müller, C., Charniga, C., Temple, S. & Finnemann, S. C. Quantified F-Actin Morphology Is Predictive of Phagocytic Capacity of Stem Cell-Derived Retinal Pigment Epithelium. *Stem Cell Rep* **10**, 1075–1087 (2018).

41. Oberst, A. *et al.* Inducible Dimerization and Inducible Cleavage Reveal a Requirement for Both Processes in Caspase-8 Activation*. *J. Biol. Chem.* **285**, 16632–16642 (2010).

42. Ko, F. *et al.* Associations with Retinal Pigment Epithelium Thickness Measures in a Large Cohort Results from the UK Biobank. *Ophthalmology* **124**, 105–117 (2017).

43. Bonilha, V. L., Rayborn, M. E., Saotome, I., McClatchey, A. I. & Hollyfield, J. G. Microvilli defects in retinas of ezrin knockout mice. *Exp. Eye Res.* **82**, 720–729 (2006).

44. Kivelä, T., Jääskeläinen, J., Vaheri, A. & Carpén, O. Ezrin, a membrane-organizing protein, as a polarization marker of the retinal pigment epithelium in vertebrates. *Cell Tissue Res.* **301**, 217–223 (2000).

45. Bonilha, V. L., Finnemann, S. C. & Rodriguez-Boulan, E. Ezrin Promotes Morphogenesis of Apical Microvilli and Basal Infoldings in Retinal Pigment Epithelium. *J. Cell Biol.* **147**, 1533–1548 (1999).

46. Fievet, B. T. *et al.* Phosphoinositide binding and phosphorylation act sequentially in the activation mechanism of ezrin. *J. Cell Biol.* **164**, 653–659 (2004).

47. Tixeira, R. *et al.* Defining the morphologic features and products of cell disassembly during apoptosis. *Apoptosis* **22**, 475–477 (2017).

48. Zihni, C. Phagocytosis by the retinal pigment epithelium: New insights into polarized cell mechanics. *BioEssays* **47**, e2300197 (2025).

49. Umapathy, A. *et al.* Spatiotemporal Live-Cell Analysis of Photoreceptor Outer Segment Membrane Ingestion by the Retinal Pigment Epithelium Reveals Actin-Regulated Scission. *J. Neurosci.* **43**, 2653–2664 (2023).

50. Kozyrina, A. N. *et al.* Laminin-defined mechanical status modulates retinal pigment epithelium phagocytosis. *EMBO Rep.* 1–27 (2025) doi:10.1038/s44319-025-00475-9.

51. Ma, J. Y. W. *et al.* Aging induces cell loss and a decline in phagosome processing in the mouse retinal pigment epithelium. *Neurobiol. Aging* **128**, 1–16 (2023).

52. Kwon, W. & Freeman, S. A. Phagocytosis by the Retinal Pigment Epithelium: Recognition, Resolution, Recycling. *Front Immunol* **11**, 604205 (2020).

53. Olson, E. N. & Nordheim, A. Linking actin dynamics and gene transcription to drive cellular motile functions. *Nat. Rev. Mol. Cell Biol.* **11**, 353–365 (2010).

54. Cai, H., Fields, M. A., Hoshino, R. & Priore, L. V. D. Effects of Aging and Anatomic Location on Gene Expression in Human Retina. *Front. Aging Neurosci.* **4**, 8 (2012).

55. Butler, J. M., Supharattanasitthi, W., Yang, Y. C. & Paraoan, L. RNA-seq analysis of ageing human retinal pigment epithelium: Unexpected up-regulation of visual cycle gene transcription. *J. Cell. Mol. Med.* **25**, 5572–5585 (2021).

56. Chaudhuri, O. Viscoelastic hydrogels for 3D cell culture. *Biomater. Sci.* **5**, 1480–1490 (2017).

57. Khalilgharibi, N. *et al.* Stress relaxation in epithelial monolayers is controlled by the actomyosin cortex. *Nat. Phys.* **15**, 839–847 (2019).

58. Nagayama, M., Haga, H., Takahashi, M., Saitoh, T. & Kawabata, K. Contribution of cellular contractility to spatial and temporal variations in cellular stiffness. *Exp. Cell Res.* **300**, 396–405 (2004).

59. Wang, N. *et al.* Cell prestress. I. Stiffness and prestress are closely associated in adherent contractile cells. *Am. J. Physiol.-Cell Physiol.* **282**, C606–C616 (2002).

60. Watanabe, T., Hosoya, H. & Yonemura, S. Regulation of Myosin II Dynamics by Phosphorylation and Dephosphorylation of Its Light Chain in Epithelial Cells. *Mol. Biol. Cell* **18**, 605–616 (2007).

61. Leerberg, J. M. & Yap, A. S. Vinculin, cadherin mechanotransduction and homeostasis of cell–cell junctions. *Protoplasma* **250**, 817–829 (2013).

62. Brückner, B. R. & Janshoff, A. Importance of integrity of cell-cell junctions for the mechanics of confluent MDCK II cells. *Sci. Rep.* **8**, 14117 (2018).

63. Prevedel, R., Diz-Muñoz, A., Ruocco, G. & Antonacci, G. Brillouin microscopy: an emerging tool for mechanobiology. *Nat Methods* **16**, 969–977 (2019).

64. Passeri, A. A. *et al.* Beyond Water Content: Unraveling Stiffness in Hydrated Materials by a Correlative Brillouin–Raman Approach. *ACS Photonics* **12**, 3794–3802 (2025).

65. Geisler, F. *et al.* Intestinal intermediate filament polypeptides in C. elegans: Common and isotype-specific contributions to intestinal ultrastructure and function. *Sci. Rep.* **10**, 3142 (2020).

66. Chugh, P. *et al.* Actin cortex architecture regulates cell surface tension. *Nat. cell Biol.* **19**, 689–697 (2017).

67. Lee, S. Y., Fujioka, T., Osuga, M., Nishimura, T. & Suetsugu, S. Plasma Membrane Shaping. 245–263 (2023) doi:10.1016/b978-0-323-89911-6.00019-4.

68. Hetrick, B., Han, M. S., Helgeson, L. A. & Nolen, B. J. Small Molecules CK-666 and CK-869 Inhibit Actin-Related Protein 2/3 Complex by Blocking an Activating Conformational Change. *Chem. Biol.* **20**, 701–712 (2013).

69. Rizvi, S. A. *et al.* Identification and Characterization of a Small Molecule Inhibitor of Formin-Mediated Actin Assembly. *Chem. Biol.* **16**, 1158–1168 (2009).

70. Nishimura, Y. *et al.* The Formin Inhibitor, SMIFH2, Inhibits Members of the Myosin Superfamily. *J. Cell Sci.* **134**, jcs.253708 (2021).

71. Pomatto, L. C. D. & Davies, K. J. A. The role of declining adaptive homeostasis in ageing. *J. Physiol.* **595**, 7275–7309 (2017).

72. Schmauck-Medina, T. *et al.* New hallmarks of ageing: a 2022 Copenhagen ageing meeting summary. *Aging* **14**, 6829–6839 (2022).

73. Cornacchia, D. & Studer, L. Back and forth in time: Directing age in iPSC-derived lineages. *Brain Res.* **1656**, 14–26 (2017).

74. Bonilha, V. L. Age and disease-related structural changes in the retinal pigment epithelium. *Clin Ophthalmol Auckl N Z* **2**, 413–424 (2008).

75. Chen, M. *et al.* Retinal pigment epithelial cell multinucleation in the aging eye – a mechanism to repair damage and maintain homoeostasis. *Aging Cell* **15**, 436–445 (2016).

76. Tamori, Y. & Deng, W.-M. Compensatory cellular hypertrophy: the other strategy for tissue homeostasis. *Trends Cell Biol* **24**, 230–237 (2014).

77. Bodenschatz, J. F. E. *et al.* Epithelial cells sacrifice excess area to preserve fluidity in response to external mechanical stress. *Commun. Biol.* **5**, 855 (2022).

78. Figard, L., Wang, M., Zheng, L., Golding, I. & Sokac, A. M. Membrane Supply and Demand Regulates F-Actin in a Cell Surface Reservoir. *Dev. Cell* **37**, 267–278 (2016).

79. Liao, M. *et al.* Multi-omics profiling of retinal pigment epithelium reveals enhancer-driven activation of RANK-NFATc1 signaling in traumatic proliferative vitreoretinopathy. *Nat. Commun.* **15**, 7324 (2024).

80. Zhang, Q. *et al.* Comparison of histologic findings in age-related macular degeneration with RPE flatmount images. *Mol. Vis.* **25**, 70–78 (2019).

81. Trepat, X. *et al.* Viscoelasticity of human alveolar epithelial cells subjected to stretch. *Am. J. Physiol.-Lung Cell. Mol. Physiol.* **287**, L1025–L1034 (2004).

82. Morris, T., Sue, E., Geniesse, C., Brieher, W. M. & Tang, V. W. Synaptopodin stress fiber and contractomere at the epithelial junction. *J. Cell Biol.* **221**, e202011162 (2022).

83. López-Gay, J. M. *et al.* Apical stress fibers enable a scaling between cell mechanical response and area in epithelial tissue. *Science* **370**, eabb2169 (2020).

84. Bays, J. L., Campbell, H. K., Heidema, C., Sebbagh, M. & DeMali, K. A. Linking E-cadherin mechanotransduction to cell metabolism through force-mediated activation of AMPK. *Nat. Cell Biol.* **19**, 724–731 (2017).

85. Gutmann, M. *et al.* Beyond comparison: Brillouin microscopy and AFM-based indentation reveal divergent insights into the mechanical profile of the murine retina. *J. Phys.: Photonics* **6**, 035020 (2024).

86. Zhang, P., Medwig-Kinney, T. N. & Goldstein, B. Architecture of the cortical actomyosin network driving apical constriction in C. elegans. *J. Cell Biol.* **222**, e202302102 (2023).

87. Brückner, B. R., Pietuch, A., Nehls, S., Rother, J. & Janshoff, A. Ezrin is a Major Regulator of Membrane Tension in Epithelial Cells. *Sci. Rep.* **5**, 14700 (2015).

88. Goodwin, K. *et al.* Cell–cell and cell–extracellular matrix adhesions cooperate to organize actomyosin networks and maintain force transmission during dorsal closure. *Mol. Biol. Cell* **28**, 1301–1310 (2017).

89. Maruthamuthu, V., Sabass, B., Schwarz, U. S. & Gardel, M. L. Cell-ECM traction force modulates endogenous tension at cell–cell contacts. *Proc National Acad Sci* **108**, 4708–4713 (2011).

90. Valencia-Expósito, A., Khalilgharibi, N., Millán, A. M.-A., Mao, Y. & Martín-Bermudo, M. D. Local weakening of cell-extracellular matrix adhesion triggers basal epithelial tissue folding. *EMBO J.* **44**, 2002–2024 (2025).

91. Zuidema, A., Wang, W. & Sonnenberg, A. Crosstalk between Cell Adhesion Complexes in Regulation of Mechanotransduction. *BioEssays* **42**, 2000119 (2020).

92. Mui, K. L., Chen, C. S. & Assoian, R. K. The mechanical regulation of integrin–cadherin crosstalk organizes cells, signaling and forces. *J Cell Sci* **129**, 1093–1100 (2016).

93. Weber, G. F., Bjerke, M. A. & DeSimone, D. W. Integrins and cadherins join forces to form adhesive networks. *J Cell Sci* **124**, 1183–93 (2011).

94. Rooij, J. de, Kerstens, A., Danuser, G., Schwartz, M. A. & Waterman-Storer, C. M. Integrin-dependent actomyosin contraction regulates epithelial cell scattering. *J. Cell Biol.* **171**, 153–164 (2005).

95. Herant, M., Heinrich, V. & Dembo, M. Mechanics of neutrophil phagocytosis: behavior of the cortical tension. *J. Cell Sci.* **118**, 1789–1797 (2005).

96. Herant, M., Heinrich, V. & Dembo, M. Mechanics of neutrophil phagocytosis: experiments and quantitative models. *J. Cell Sci.* **119**, 1903–1913 (2006).

97. Vorselen, D., Labitigan, R. L. D. & Theriot, J. A. A mechanical perspective on phagocytic cup formation. *Curr Opin Cell Biol* **66**, 112–122 (2020).

98. Hoijman, E. *et al.* Cooperative epithelial phagocytosis enables error correction in the early embryo. *Nature* **590**, 618–623 (2021).

99. Li, J. X. H., Tang, V. W. & Brieher, W. M. Actin protrusions push at apical junctions to maintain E-cadherin adhesion. *Proc. Natl. Acad. Sci.* **117**, 432–438 (2020).

100. Gao, H. & Hollyfield, J. G. Aging of the human retina. Differential loss of neurons and retinal pigment epithelial cells. *Invest Ophth Vis Sci* **33**, 1–17 (1992).

101. Curcio, C. A., Millican, C. L., Allen, K. A. & Kalina, R. E. Aging of the human photoreceptor mosaic: evidence for selective vulnerability of rods in central retina. *Investig. Ophthalmol. Vis. Sci.* **34**, 3278–96 (1993).

102. Curcio, C. A. & Drucker, D. N. Retinal ganglion cells in Alzheimer's disease and aging. *Ann. Neurol.* **33**, 248–257 (1993).

103. Eliasieh, K., Liets, L. C. & Chalupa, L. M. Cellular Reorganization in the Human Retina during Normal Aging. *Investig. Opthalmology Vis. Sci.* **48**, 2824 (2007).

104. Tse, J. R. & Engler, A. J. Preparation of Hydrogel Substrates with Tunable Mechanical Properties. *Curr. Protoc. Cell Biol.* **47**, 10.16.1-10.16.16 (2010).

105. Przybyla, L., Lakins, J. N., Sunyer, R., Trepat, X. & Weaver, V. M. Monitoring developmental force distributions in reconstituted embryonic epithelia. *Methods* **94**, 101–113 (2016).

106. Parinot, C., Rieu, Q., Chatagnon, J., Finnemann, S. C. & Nandrot, E. F. Large-Scale Purification of Porcine or Bovine Photoreceptor Outer Segments for Phagocytosis Assays on Retinal Pigment Epithelial Cells. *J. Vis. Exp.* (2014) doi:10.3791/52100.

107. Schindelin, J. *et al.* Fiji: an open-source platform for biological-image analysis. *Nat. Methods* **9**, 676–682 (2012).

108. Ewels, P. A. *et al.* The nf-core framework for community-curated bioinformatics pipelines. *Nat. Biotechnol.* **38**, 276–278 (2020).

109. Tommaso, P. D. *et al.* Nextflow enables reproducible computational workflows. *Nat. Biotechnol.* **35**, 316–319 (2017).

110. Love, M. I., Huber, W. & Anders, S. Moderated estimation of fold change and dispersion for RNA-seq data with DESeq2. *Genome Biol.* **15**, 550 (2014).

111. Kolde, R. *Pheatmap: Pretty Heatmaps*. (2018).

112. Raudvere, U. *et al.* g:Profiler: a web server for functional enrichment analysis and conversions of gene lists (2019 update). *Nucleic Acids Res.* **47**, W191–W198 (2019).

113. Janes, K. A. An analysis of critical factors for quantitative immunoblotting. *Sci. Signal.* **8**, rs2 (2015).

114. LAEMMLI, U. K. Cleavage of Structural Proteins during the Assembly of the Head of Bacteriophage T4. *Nature* **227**, 680–685 (1970).

115. Brunelle, J. L. & Green, R. One-dimensional SDS-polyacrylamide gel electrophoresis (1D SDS-PAGE). *Methods Enzym.* **541**, 151–9 (2014).

116. Stringer, C., Wang, T., Michaelos, M. & Pachitariu, M. Cellpose: a generalist algorithm for cellular segmentation. *Nat. Methods* **18**, 100–106 (2021).

117. Bi, D., Lopez, J. H., Schwarz, J. M. & Manning, M. L. A density-independent rigidity transition in biological tissues. *Nat. Phys.* **11**, 1074–1079 (2015).

118. Park, J.-A. *et al.* Unjamming and cell shape in the asthmatic airway epithelium. *Nat. Mater.* **14**, 1040–1048 (2015).

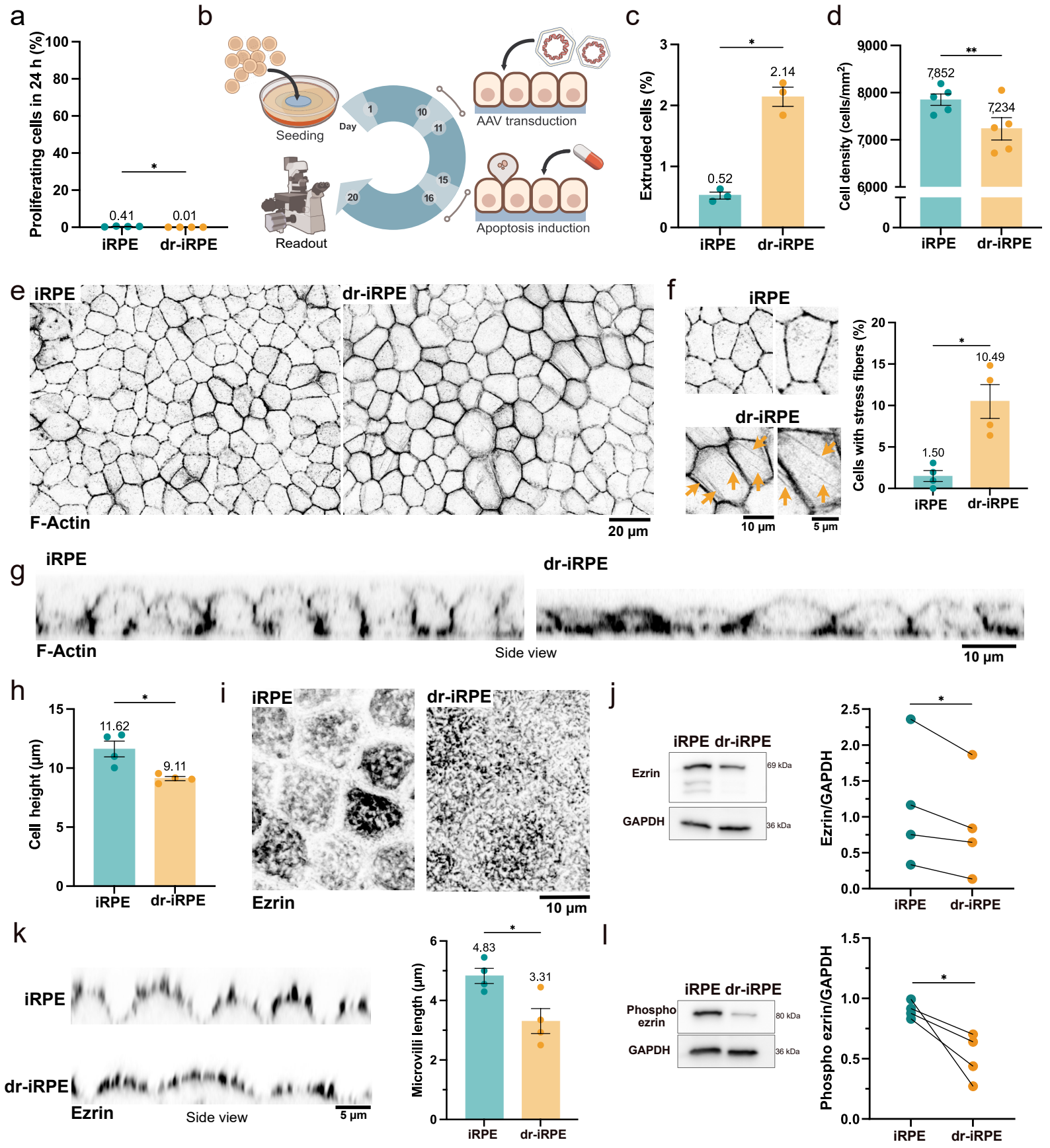
a
Proliferating cells in 24 h (%)
100
80
60
40
20
0
*
0.41
0.01
iRPE
dr-iRPE
b
Seeding
Day
1
10
11
15
16
20
Readout
AAV transduction
Apoptosis induction
c
Extruded cells (%)
3
2
1
0
*
2.14
0.52
iRPE
dr-iRPE
d
Cell density (cells/mm²)
9,000
8,000
7,000
6,000
0
**
7,852
7,234
iRPE
dr-iRPE
e
iRPE
dr-iRPE
F-Actin
20 µm
f
iRPE
dr-iRPE
10 µm
5 µm
Cells with stress fibers (%)
20
15
10
5
0
*
10.49
1.50
iRPE
dr-iRPE
g
iRPE
dr-iRPE
F-Actin
Side view
10 µm
h
Cell height (µm)
15
10
5
0
*
11.62
9.11
iRPE
dr-iRPE
i
iRPE
dr-iRPE
Ezrin
10 µm
j
iRPE dr-iRPE
Ezrin
69 kDa
GAPDH
36 kDa
Ezrin/GAPDH
2.5
2.0
1.5
1.0
0.5
0.0
*
iRPE
dr-iRPE
k
iRPE
dr-iRPE
Ezrin
Side view
5 µm
Microvilli length (µm)
6
4
2
0
*
4.83
3.31
iRPE
dr-iRPE
l
iRPE dr-iRPE
Phospho ezrin
80 kDa
GAPDH
36 kDa
Phospho ezrin/GAPDH
1.5
1.0
0.5
0.0
*
iRPE
dr-iRPE

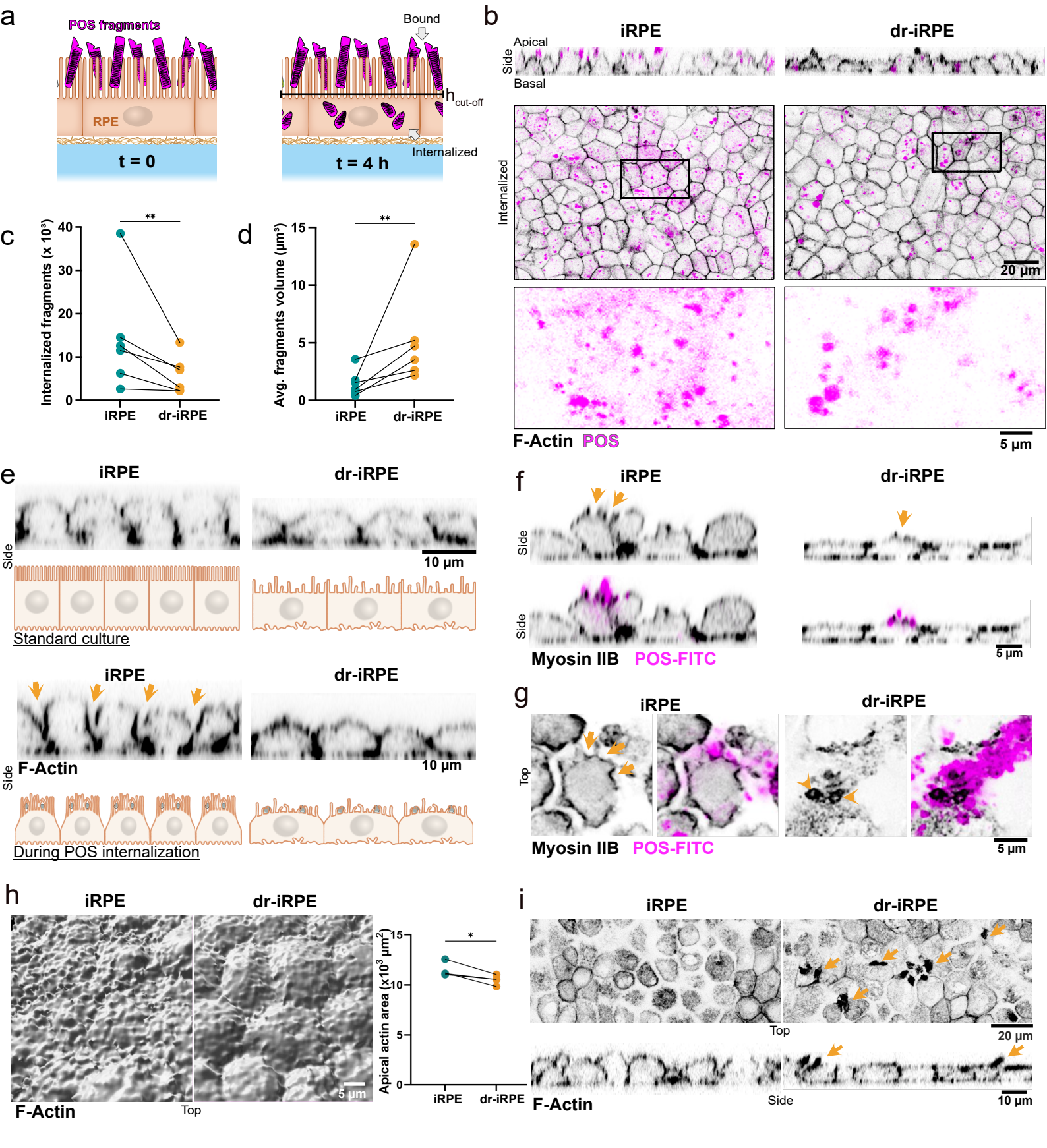
a
POS fragments
RPE
t = 0
Bound
h cut-off
Internalized
t = 4 h
b
iRPE
dr-iRPE
Apical
Side
Basal
Internalized
20 µm
F-Actin POS
5 µm
c
Internalized fragments (x 10³)
iRPE
dr-iRPE
d
Avg. fragments volume (µm³)
iRPE
dr-iRPE
e
iRPE
dr-iRPE
Side
10 µm
Standard culture
iRPE
dr-iRPE
F-Actin
Side
10 µm
During POS internalization
f
iRPE
dr-iRPE
Side
Side
Myosin IIB POS-FITC
5 µm
g
iRPE
dr-iRPE
Top
Myosin IIB POS-FITC
5 µm
h
iRPE
dr-iRPE
5 µm
F-Actin
Top
Apical actin area (x10³ µm²)
iRPE
dr-iRPE
i
iRPE
dr-iRPE
Top
20 µm
F-Actin
Side
10 µm

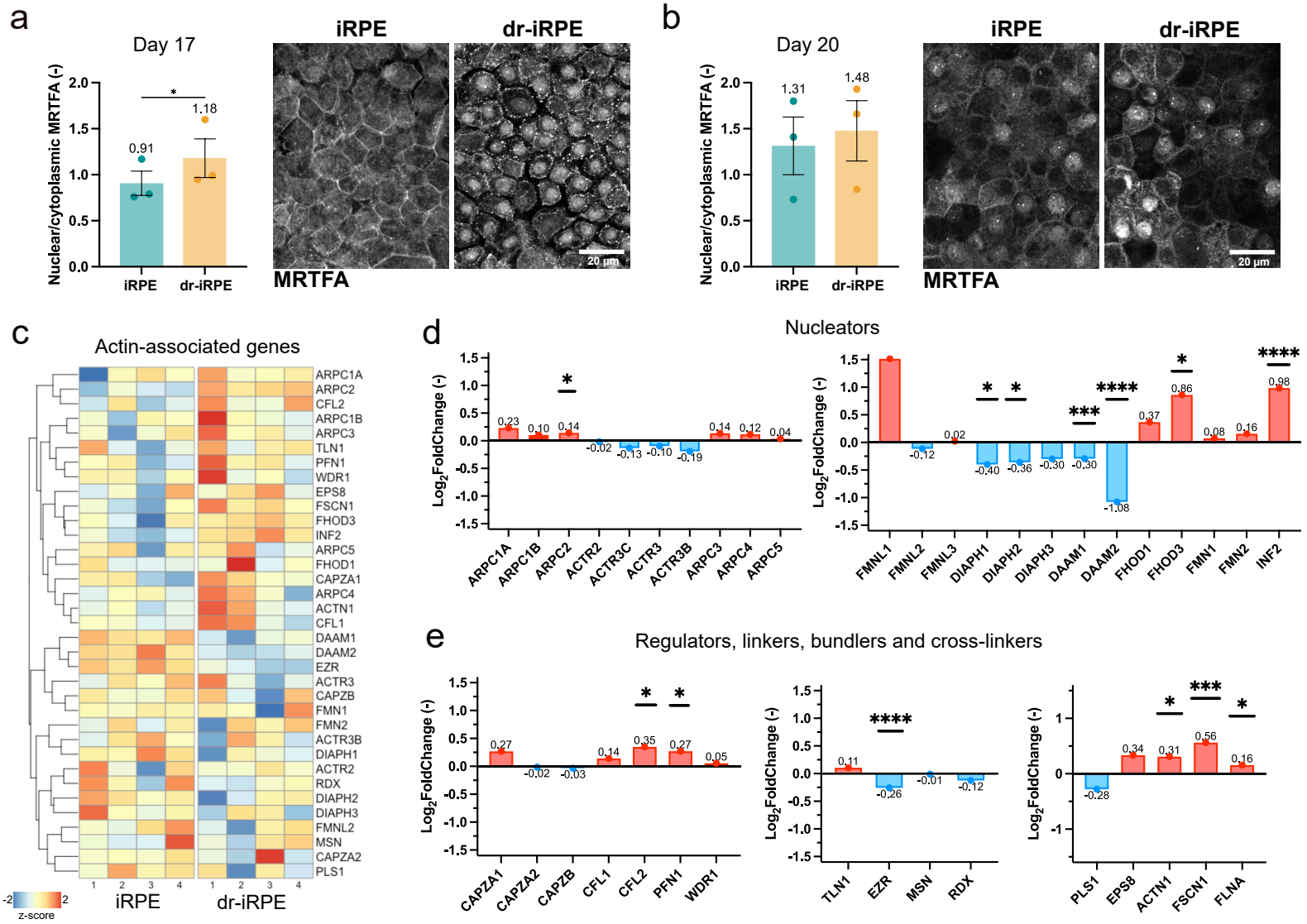
a
Day 17
Nuclear/cytoplasmic MRTFA (-)
2.0
1.5
1.0
0.5
0.0
*
0.91
1.18
iRPE
dr-iRPE
iRPE
dr-iRPE
MRTFA
20 µm
b
Day 20
Nuclear/cytoplasmic MRTFA (-)
1.31
1.48
iRPE
dr-iRPE
iRPE
dr-iRPE
MRTFA
20 µm
c
Actin-associated genes
ARPC1A
ARPC2
CFL2
ARPC1B
ARPC3
TLN1
PFN1
WDR1
EPS8
FSCN1
FHOD3
INF2
ARPC5
FHOD1
CAPZA1
ARPC4
ACTN1
CFL1
DAAM1
DAAM2
EZR
ACTR3
CAPZB
FMN1
FMN2
ACTR3B
DIAPH1
ACTR2
RDX
DIAPH2
DIAPH3
FMNL2
MSN
CAPZA2
PLS1
1 2 3 4
iRPE
1 2 3 4
dr-iRPE
-2
2
z-score
d
Nucleators
Log2FoldChange (-)
1.5
1.0
0.5
0.0
-0.5
-1.0
-1.5
*
0.23
0.10
0.14
-0.02
-0.13
-0.10
-0.19
0.14
0.12
0.04
ARPC1A
ARPC1B
ARPC2
ACTR2
ACTR3C
ACTR3
ACTR3B
ARPC3
ARPC4
ARPC5
*
*
***
****
*
****
0.02
-0.12
-0.40
-0.36
-0.30
-0.30
-1.08
0.37
0.86
0.08
0.16
0.98
FMNL1
FMNL2
FMNL3
DIAPH1
DIAPH2
DIAPH3
DAAM1
DAAM2
FHOD1
FHOD3
FMN1
FMN2
INF2
e
Regulators, linkers, bundlers and cross-linkers
Log2FoldChange (-)
*
*
0.27
-0.02
-0.03
0.14
0.35
0.27
0.05
CAPZA1
CAPZA2
CAPZB
CFL1
CFL2
PFN1
WDR1
****
0.11
-0.26
-0.01
-0.12
TLN1
EZR
MSN
RDX
*
***
*
-0.28
0.34
0.31
0.56
0.16
PLS1
EPS8
ACTN1
FSCN1
FLNA

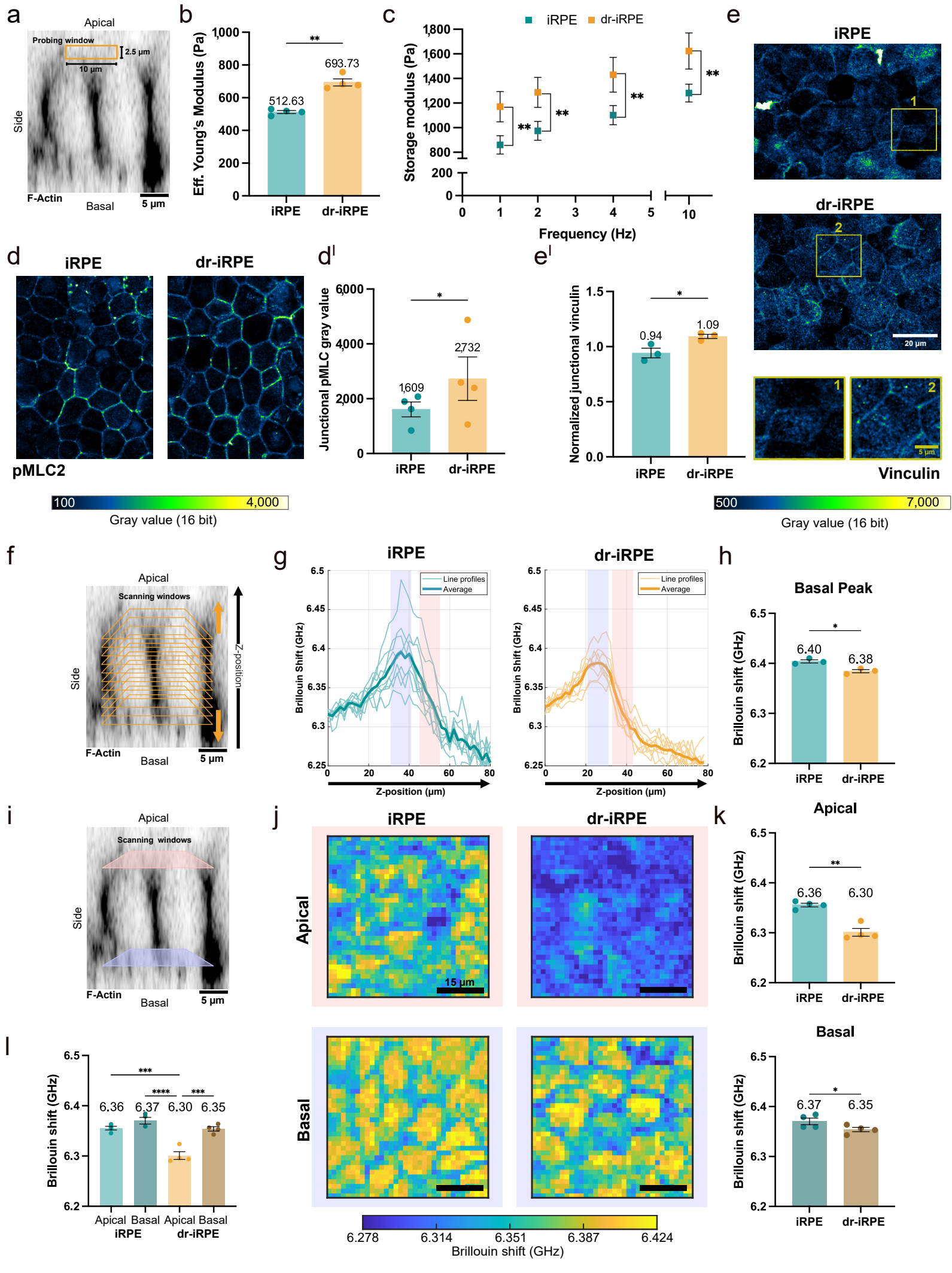
a
Apical
Probing window
2.5 µm
10 µm
Side
F-Actin
Basal
5 µm
b
Eff. Young's Modulus (Pa)
1,000
800
600
400
200
0
**
512.63
693.73
iRPE
dr-iRPE
c
iRPE
dr-iRPE
Storage modulus (Pa)
1,800
1,600
1,400
1,200
1,000
800
200
0
**
**
**
**
0
1
2
3
4
5
10
Frequency (Hz)
e
iRPE
1
dr-iRPE
2
20 µm
1
2
5 µm
Vinculin
500
7,000
Gray value (16 bit)
d
iRPE
dr-iRPE
pMLC2
100
4,000
Gray value (16 bit)
d'
Junctional pMLC gray value
6,000
4,000
2,000
0
*
1,609
2,732
iRPE
dr-iRPE
e'
Normalized junctional vinculin
1.5
1.0
0.5
0.0
*
0.94
1.09
iRPE
dr-iRPE
f
Apical
Scanning windows
Side
Z-position
F-Actin
Basal
5 µm
g
iRPE
Line profiles
Average
Brillouin Shift (GHz)
6.5
6.45
6.4
6.35
6.3
6.25
0
20
40
60
80
Z-position (µm)
dr-iRPE
Line profiles
Average
Brillouin Shift (GHz)
6.5
6.45
6.4
6.35
6.3
6.25
0
20
40
60
80
Z-position (µm)
h
Basal Peak
Brillouin shift (GHz)
6.5
6.4
6.3
6.2
*
6.40
6.38
iRPE
dr-iRPE
i
Apical
Scanning windows
Side
F-Actin
Basal
5 µm
j
iRPE
dr-iRPE
Apical
15 µm
Basal
6.278
6.314
6.351
6.387
6.424
Brillouin shift (GHz)
k
Apical
Brillouin shift (GHz)
6.5
6.4
6.3
6.2
**
6.36
6.30
iRPE
dr-iRPE
Basal
Brillouin shift (GHz)
6.5
6.4
6.3
6.2
*
6.37
6.35
iRPE
dr-iRPE
l
Brillouin shift (GHz)
6.5
6.4
6.3
6.2
***
****
***
6.36
6.37
6.30
6.35
Apical
Basal
Apical
Basal
iRPE
dr-iRPE

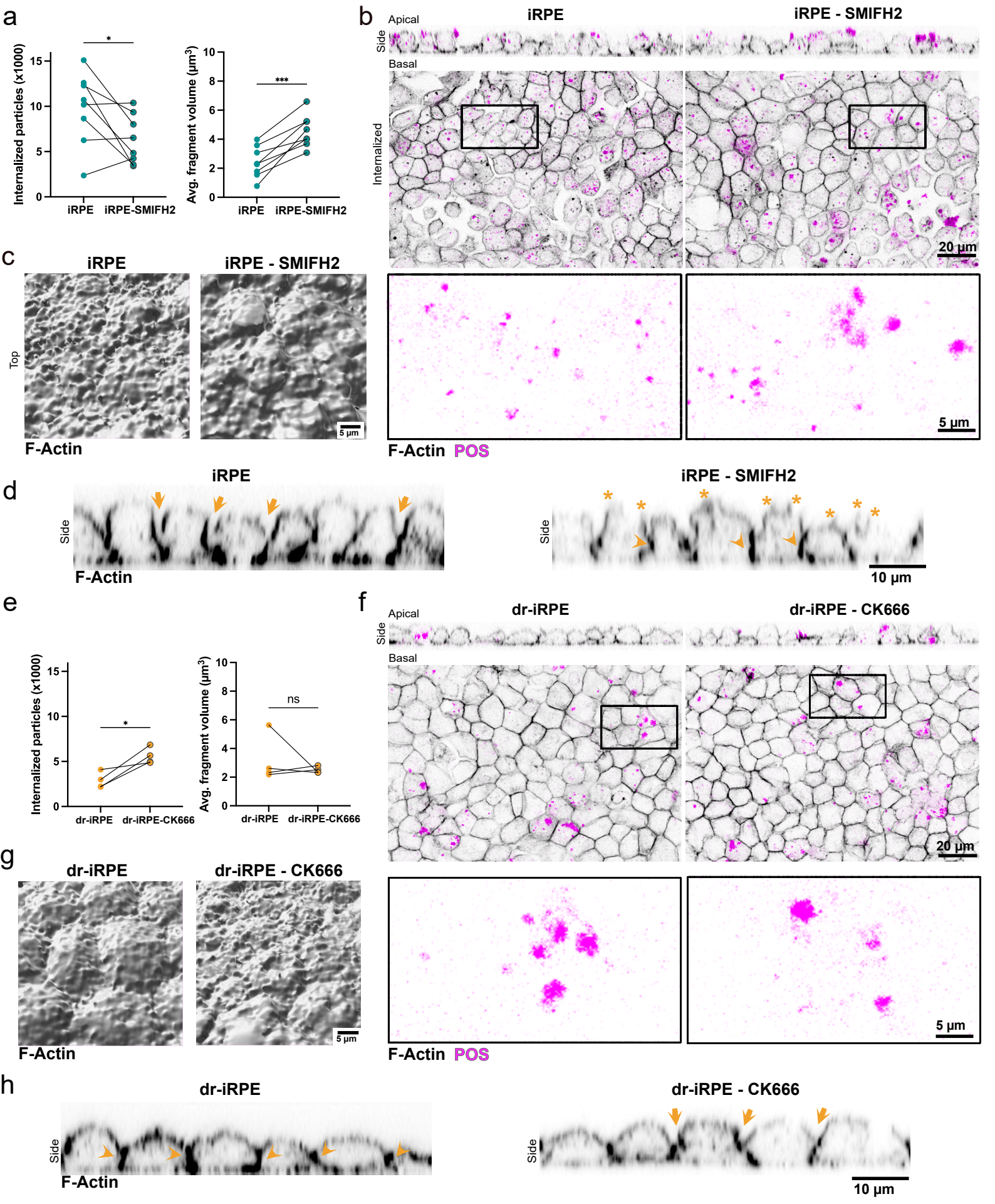
a
Internalized particles (x1000)
iRPE
iRPE-SMIFH2
Avg. fragment volume (µm³)
b
Apical
Side
Basal
Internalized
iRPE
iRPE - SMIFH2
20 µm
5 µm
F-Actin
POS
c
Top
iRPE
iRPE - SMIFH2
5 µm
F-Actin
d
iRPE
iRPE - SMIFH2
Side
F-Actin
10 µm
e
Internalized particles (x1000)
dr-iRPE
dr-iRPE-CK666
Avg. fragment volume (µm³)
ns
f
Apical
Side
Basal
dr-iRPE
dr-iRPE - CK666
20 µm
5 µm
F-Actin
POS
g
dr-iRPE
dr-iRPE - CK666
5 µm
F-Actin
h
dr-iRPE
dr-iRPE - CK666
Side
F-Actin
10 µm

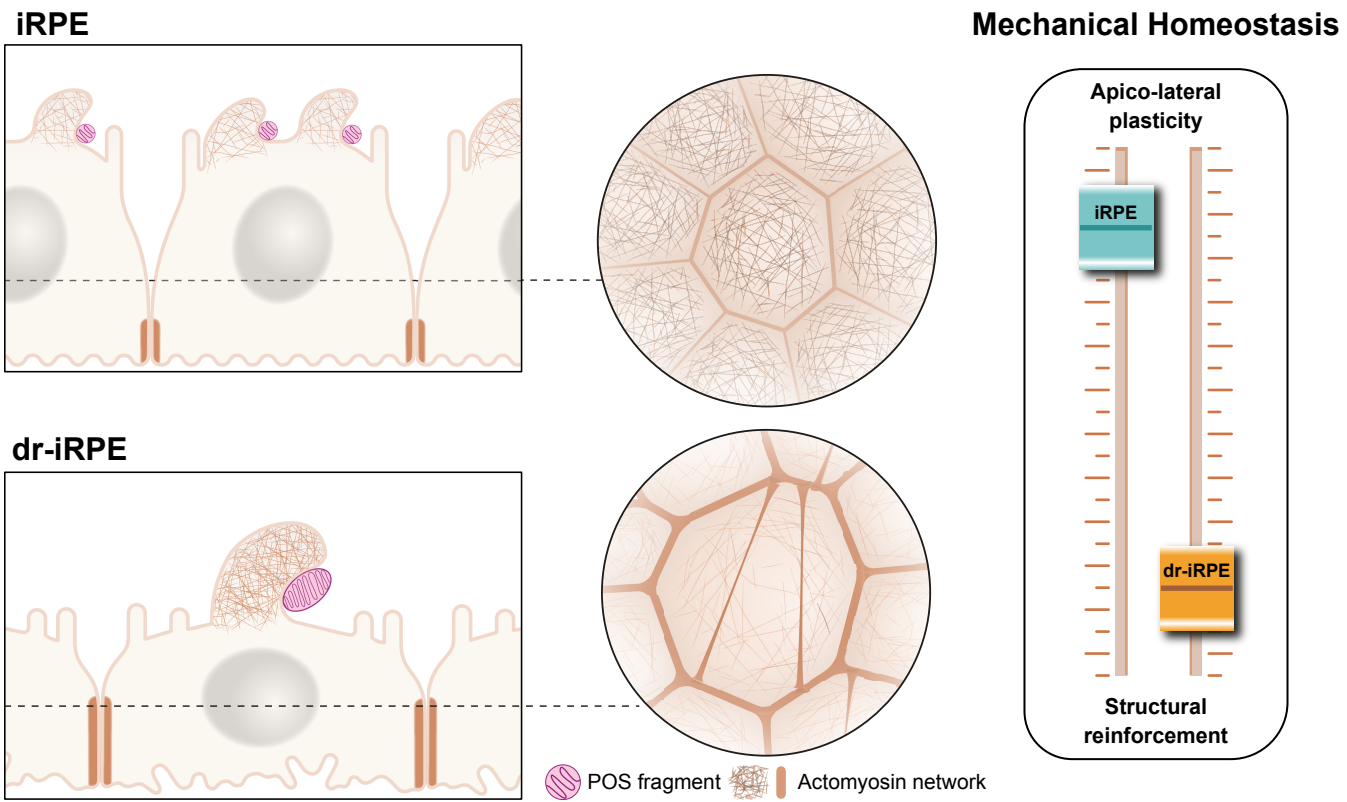
iRPE
dr-iRPE
Mechanical Homeostasis
Apico-lateral plasticity
iRPE
dr-iRPE
Structural reinforcement
POS fragment
Actomyosin network